

Satellite observed trends of global mean net atmospheric shortwave and longwave irradiances and diabatic heating by precipitation

Article

Published Version

Creative Commons: Attribution-Noncommercial 4.0

Open Access

Kato, S. ORCID: https://orcid.org/0000-0001-7597-0886, Thorsen, T. J. ORCID: https://orcid.org/0000-0002-4405-3572, Rose, F. G., Loeb, N. G. ORCID: https://orcid.org/0000-0002-2538-9644, Ham, S.-H., Rutan, D. A., Li, Z., Mayer, M., Allan, R. P. ORCID: https://orcid.org/0000-0003-0264-9447, Adler, R. F. ORCID: https://orcid.org/0000-0002-6945-8242, Gu, G. ORCID: https://orcid.org/0000-0001-6219-8006, Lee, S. ORCID: https://orcid.org/0000-0003-2821-1208 and Lee, J. ORCID: https://orcid.org/0000-0002-5029-476X (2025) Satellite observed trends of global mean net atmospheric shortwave and longwave irradiances and diabatic heating by precipitation. Science Advances, 11 (42). ISSN 2375-2548 doi: 10.1126/sciadv.adz1292 Available at https://centaur.reading.ac.uk/125199/

It is advisable to refer to the publisher's version if you intend to cite from the work. See <u>Guidance on citing</u>.

Published version at: https://doi.org/10.1126/sciadv.adz1292

To link to this article DOI: http://dx.doi.org/10.1126/sciadv.adz1292



Publisher: AAAS

All outputs in CentAUR are protected by Intellectual Property Rights law, including copyright law. Copyright and IPR is retained by the creators or other copyright holders. Terms and conditions for use of this material are defined in the End User Agreement.

www.reading.ac.uk/centaur

CentAUR

Central Archive at the University of Reading

Reading's research outputs online

Check for updates

ATMOSPHERIC SCIENCE

Satellite observed trends of global mean net atmospheric shortwave and longwave irradiances and diabatic heating by precipitation

Seiji Kato¹*, Tyler J. Thorsen¹, Fred G. Rose², Norman G. Loeb¹, Seung-Hee Ham¹, David A. Rutan³, Zhujun Li², Michael Mayer^{4,5}, Richard P. Allan⁶, Robert F. Adler⁷, Guojun Gu⁷, Seoyoung Lee⁸, Jaehwa Lee⁷

The changes in global mean precipitation over recent decades are poorly understood despite their fundamental importance to climate change prediction. We provide an observational verification of the physical link between global precipitation and net atmospheric radiative cooling. April 2006 through December 2024, the net atmospheric total (shortwave + longwave) cooling increases at a rate of 0.11 ± 0.31 watts per square meter per decade (Wm⁻² dec⁻¹). Trends of longwave cooling and shortwave heating are 0.76 ± 0.48 and 0.64 ± 0.27 Wm⁻² dec⁻¹, respectively. The longwave trend is a result of partial cancelation among contributions from increasing surface skin temperature, air temperature, and water vapor. Increasing shortwave absorption is caused by increasing water vapor. The trend of global mean diabatic heating by precipitation is 0.03 ± 0.61 Wm⁻² dec⁻¹. These results observationally confirm that an absence of current global precipitation trends is consistent with net atmospheric radiative cooling trends explained by nearly balanced changes between longwave cooling and shortwave heating.

Copyright © 2025 The Authors, some rights reserved; exclusive licensee American Association for the Advancement of Science. No claim to original U.S.
Government Works.
Distributed under a Creative Commons Attribution
NonCommercial
License 4.0 (CC BY-NC).

INTRODUCTION

Atmosphere absorbs solar irradiances primarily due to absorption by water vapor in the atmosphere. Atmosphere also absorbs radiation emitted by the surface. In addition, atmosphere emits radiation to the surface and space. When these irradiances are averaged globally over a year, the climatological value of the absorbed solar by the atmosphere is 77 Wm⁻², which leads to heating the atmosphere, and the difference of absorbed and emitted longwave to space and surface by the atmosphere is -187 Wm^{-2} , which leads to cooling the atmosphere [e.g., (1, 2)]. The absorption and emission by the atmosphere depend on temperature profiles, greenhouse gas concentrations, water phase, and aerosol. The spatial and temporal gradient of absorbed and emitted irradiance by the atmosphere drives dynamics in the atmosphere (3-6). Although earlier studies estimated global climatological irradiances (2, 7-9) and energy fluxes (1, 10-12) based on observations, relatively few studies have quantified (13) how shortwave absorption and longwave emission by the atmosphere have changed at a global scale over recent decades.

When surface temperature increases as a response to radiative forcing, water vapor in the atmosphere also increases. The rate of water vapor increase predicted by climate models (14) and observations (15) follows the Clausius-Clapeyron relationship, which is \sim 6.8% K⁻¹ for increasing near surface air temperature. Precipitation change is, however, constrained by energy balance in the atmosphere (16) and at the surface through energy fluxes' influence on evaporation [e.g., (17, 18)]. The change of global mean precipitation

¹NASA Langley Research Center, Hampton, VA, USA. ²Analytical Mechanics Associates Inc., Hampton, VA, USA. ³ADNET Systems Inc., Hampton, VA, USA. ⁴Department of Meteorology and Geophysics, University of Vienna, Vienna, Austria. ⁵Research Department, European Centre for Medium-Range Weather Forecasts, Bonn, Germany. ⁶Department of Meteorology and National Centre for Earth Observation, University of Reading, Reading, UK. ⁷Earth System Science Interdisciplinary Center, University of Maryland, Collage Park, MD, USA. ⁸Goddard Earth Sciences Technology and Research II, University of Maryland, Baltimore County, Baltimore, MD, USA. *Corresponding author. Email: seiji.kato@nasa.gov

is balanced by the change of global mean net radiative cooling in the atmosphere and surface sensible heat flux. Climate models predict the rate of global mean precipitation change of 2 to 3% K⁻¹ to a direct response to warming, but radiative forcing suppresses the increase (13). Rates of precipitation change predicted by the coupled model intercomparison project-phase5 (CMIP5) models for representative concentration pathways (RCP) 4.5 and RCP8.5 future projections have a substantial spread, but all models predict an increasing trend of precipitation (13). The increasing precipitation is also consistent with increase in global mean radiative cooling in the atmosphere predicted by CMIP5 models in a doubling CO₂ concentration scenario (19, 20).

Although climate models predict increasing precipitation in a future climate, when radiative forcing is not large, observing precipitation change is difficult, partly due to rapid adjustment to radiative forcing, which reduces atmospheric cooling, the variability of aerosol, and observational uncertainty (21). Adler et al. (22) investigated how precipitation changed from 1979 to 2014 and found that there is no statistically significant trend. Gu and Adler (23) extended the analysis through 2020 and found a slightly positive trend. Allan et al. (13) also investigated precipitation trend from 1988 to 2008 and found no significant trend. It was argued that increasing greenhouse gas concentrates in the atmosphere reduces atmospheric cooling and offsetting the increases due to stronger net atmospheric radiative cooling by a warming atmosphere [e.g., (13, 21)]. Because of this offsetting effect, Myhre et al. (20) emphasized the role of sensible heat flux in modulating global precipitation changes when radiative forcings and feedbacks approximately compensate.

Despite a robust relationship between modeled global net atmospheric total irradiance and precipitation changes, there are only a few studies addressing how global mean net atmospheric irradiance anomalies and precipitation anomalies covary observationally. Allan *et al.* (13) identified an increase in global precipitation from Global Precipitation Climatology Project (GPCP) with increasing net radiative cooling from ERA Interim of $1.1 \pm 0.2 \, \mathrm{Wm}^{-2} \, \mathrm{dec}^{-1}$ with

a correlation coefficient of 0.57 during 1988–2008 but unrealistic variability in a satellite-based estimate of radiative cooling. Naegele and Randall (24) investigated covariability of precipitation and net atmospheric total irradiance and found that the correlation coefficient is -0.7 for the tropics and +0.5 in higher latitudes. Kato *et al.* (25) investigated global monthly anomaly time series of precipitation and net atmospheric total irradiance plus anomalies of sensible heat flux and found that the correlation coefficient is -0.46.

In this study, we investigate how global mean net atmospheric shortwave, longwave, and total (shortwave + longwave) irradiances have changed since April 2006 using observations. We do not use the period from March 2000 through March 2006 because the source of sea surface temperature and sea ice concentration observations used for the Modern-Era Retrospective analysis for Research and Applications, version 2 (MERRA-2) is changed (Supplementary Text). Coarse resolution sea surface temperature and sea ice concentration sources were used before April 2006. The change influences near surface temperature near Antarctic coasts, which in turn affects surface downward longwave irradiance.

We also investigate the role of water vapor, air temperature, surface skin temperature, greenhouse gas, clouds, and aerosol in detail by analyzing their contributions in changing global net atmospheric irradiances using a partial radiative perturbation (PRP) method. In addition, we investigate how anomalies of net atmospheric total irradiance, diabatic heating by precipitation, surface sensible heat

flux, and dry static and kinetic energy tendency balance. We then show that trends of observed global mean net atmospheric total irradiance and diabatic heating of precipitation in the past ~18 years (from April 2006 through December 2024) agree to within an estimated uncertainty.

RESULTS

The sign convention of the net irradiances at top of atmosphere (TOA) and surface throughout this paper is positive downward. The net atmospheric irradiance (or radiative flux convergence) is TOA net irradiance minus surface net irradiances. A positive trend for the net atmosphere irradiance is, therefore, to warm the atmosphere, hence to reduce radiative cooling. Trends are determined by the slope of least square linear regression lines. We use 5 to 95% confidence intervals of the slope computed by the method described by Santer *et al.* (26) as the uncertainty of the trend. We do not include the uncertainty associated with retrieved cloud and aerosol properties.

Net TOA, surface, and atmosphere irradiance trend derived from Clouds and the Earth's Radiant Energy System Energy Balanced and Filled product

Figure 1 shows the time series of global monthly all-sky (A) net TOA, (B) atmospheric, and (C) surface total (shortwave plus longwave) irradiance anomalies. As investigated by Loeb *et al.* (27), the

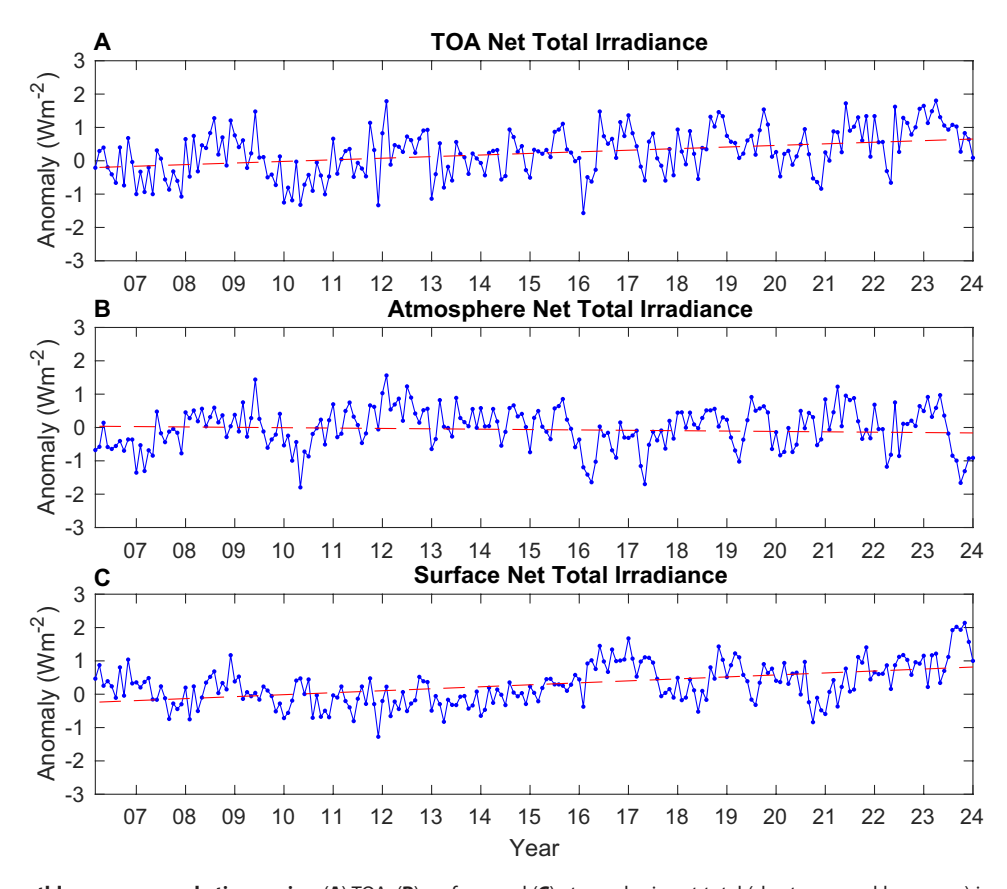


Fig. 1. All-sky global monthly mean anomaly time series. (A) TOA, (B) surface, and (C) atmospheric net total (shortwave and longwave) irradiances. A positive TOA, surface, and atmosphere net irradiance is to increase the energy flux to the Earth system, surface, and atmosphere, respectively. Anomalies are computed from July 2005 to June 2015 climatological mean. Red lines are linear regression lines.

net TOA total irradiance increases at a rate of $0.50 \pm 0.19~{\rm Wm}^{-2}~{\rm dec}^{-1}$ over the period from March 2000 through December 2023. Cloud property and surface changes are the main contributors to the increasing net TOA shortwave irradiance that dominates the net total TOA irradiance trend (27). Increasing air temperature and water vapor and decreasing clouds decrease net TOA longwave irradiance, i.e., increases outgoing longwave irradiance, in a smaller magnitude. Correlation coefficients of the net TOA total and net surface total irradiance anomalies and the net TOA total and net atmospheric total irradiance anomalies are 0.513 and 0.614, respectively.

Figure 2 summarizes global net TOA, surface, and atmospheric irradiance trends for all-sky and clear-sky conditions. Total area clear-sky irradiances [i.e., cloud removed clear-sky (28)] are used to compute clear-sky irradiance trends. The increase in the net surface total irradiance $(0.59 \pm 0.25 \ \mathrm{Wm^{-2}\ dec^{-1}})$ is faster than the increase of the net TOA irradiance of $0.48 \pm 0.24 \ \mathrm{Wm^{-2}\ dec^{-1}}$. The trend of net atmospheric total irradiance $(-0.11 \pm 0.31 \ \mathrm{Wm^{-2}\ dec^{-1}})$ is the difference between the net TOA and net surface irradiance trends. Differences between the all-sky and clear-sky trends shown in Fig. 2 are trends of cloud radiative effects on the net irradiances, which is different from cloud contributions to the net irradiance (see Partial radiative perturbation subsection in the Materials and Methods section)

The global mean all-sky net surface shortwave and longwave irradiance increases at a rate of $0.42 \pm 0.24~\rm Wm^{-2}~\rm dec^{-1}$ and $0.17 \pm 0.26~\rm Wm^{-2}~\rm dec^{-1}$, respectively. The net surface shortwave irradiance can increase via two pathways, either by increasing the downward shortwave irradiance at the surface or by decreasing the surface albedo. Decreasing cloud fraction increases the downward shortwave irradiance. Therefore, the positive trend is qualitatively consistent with the decreased cloud amount found by Loeb *et al.* (29). The positive trend is also consistent with decreasing sea ice extent [e.g., (30)], which acts to increase the fraction of downward shortwave irradiance absorbed by the ocean surface. The global mean clear-sky net surface shortwave irradiance is nearly constant, $-0.06 \pm 0.27~\rm Wm^{-2}~\rm dec^{-1}$. The global mean clear-sky net surface longwave irradiance increases at a rate of $0.38 \pm 0.25~\rm Wm^{-2}~\rm dec^{-1}$, consistent with increased

downward longwave irradiance associated with increasing atmospheric temperature and water vapor and to a lesser extent other well mixed greenhouse gases [e.g., (31, 32)].

The global mean net atmospheric shortwave irradiance increases at a rate of $0.64 \pm 0.27~{\rm Wm}^{-2}~{\rm dec}^{-1}$ for all-sky and $0.58 \pm 0.26~{\rm Wm}^{-2}$ dec⁻¹ for clear-sky conditions (Fig. 2). A smaller difference between all-sky and clear-sky conditions compared to the TOA and surface counterparts suggests that the cloud impact on the global mean net atmospheric shortwave irradiance trend is small. The global mean net atmospheric longwave irradiance is negative and changes at a rate of $-0.76 \pm 0.48~{\rm Wm}^{-2}~{\rm dec}^{-1}$ for all-sky and $-0.50 \pm 0.49~{\rm Wm}^{-2}$ dec⁻¹ for clear-sky conditions (the minus signs indicate more negative). Similar to the net atmospheric shortwave irradiances, a cloud effect on the global mean net atmospheric longwave irradiance trend is also small.

Physical reasons of the small sensitivity of the global mean net atmospheric shortwave and longwave irradiances to clouds can be understood in the following way. Net atmospheric shortwave irradiance is the irradiance absorbed by the atmosphere. Clouds can increase absorption by water vapor by increasing the path length in the atmosphere or by increasing water vapor amount and by cloud water within clouds or both (Fig. 3, A, D, and G). Cloud effects on absorbed shortwave irradiance are, however, smaller compared with cloud effects on reflected and transmitted shortwave irradiances, and effects on changes are even smaller.

For longwave, the cloud radiative effect to the atmosphere is primarily a function of cloud top height (Fig. 4B). In the tropics, warming effects by clouds at TOA is larger than cloud radiative effects at the surface (Fig. 3, D, E, and F) because often cloud heights are higher compared to the water vapor scale height of about 2 km. Over polar regions, warming effects by clouds at the surface are larger than warming effects at TOA because water vapor amounts are smaller, temperature inversion in the lower atmosphere is common (33), cloud heights are low, and high thick clouds present in tropics are absent (Fig. 4C). Longwave cooling effects also extend to stratocumulus regions because the effect of the low-level clouds at TOA is smaller than the effect at the surface, owing to a smaller difference between sea surface temperature and cloud top temperature.

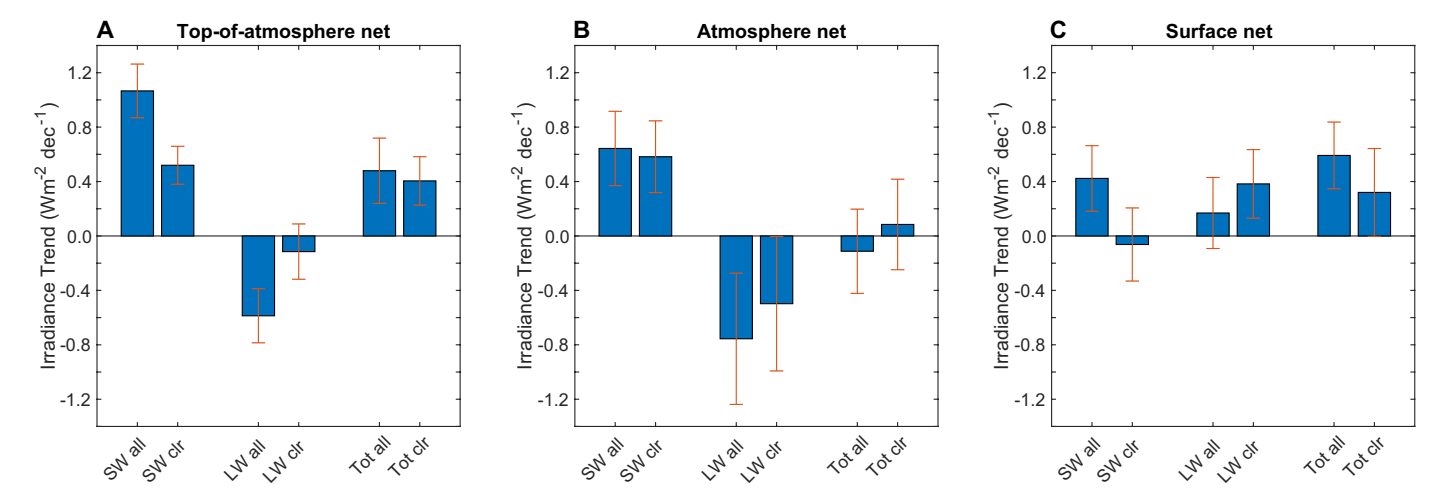


Fig. 2. Trend of global mean net irradiances over the time period from April 2006 through December 2024. (A) net TOA, (B) net atmospheric, and (C) net surface irradiances. For each panel, the left set of two bars is for shortwave (SW), the middle set is for longwave (LW), and the right set is for total (shortwave + longwave) net irradiances. For each set, the left bar is for all-sky, and the right bar is for clear-sky net irradiances. Error bars indicate 5 to 95% confidence intervals.

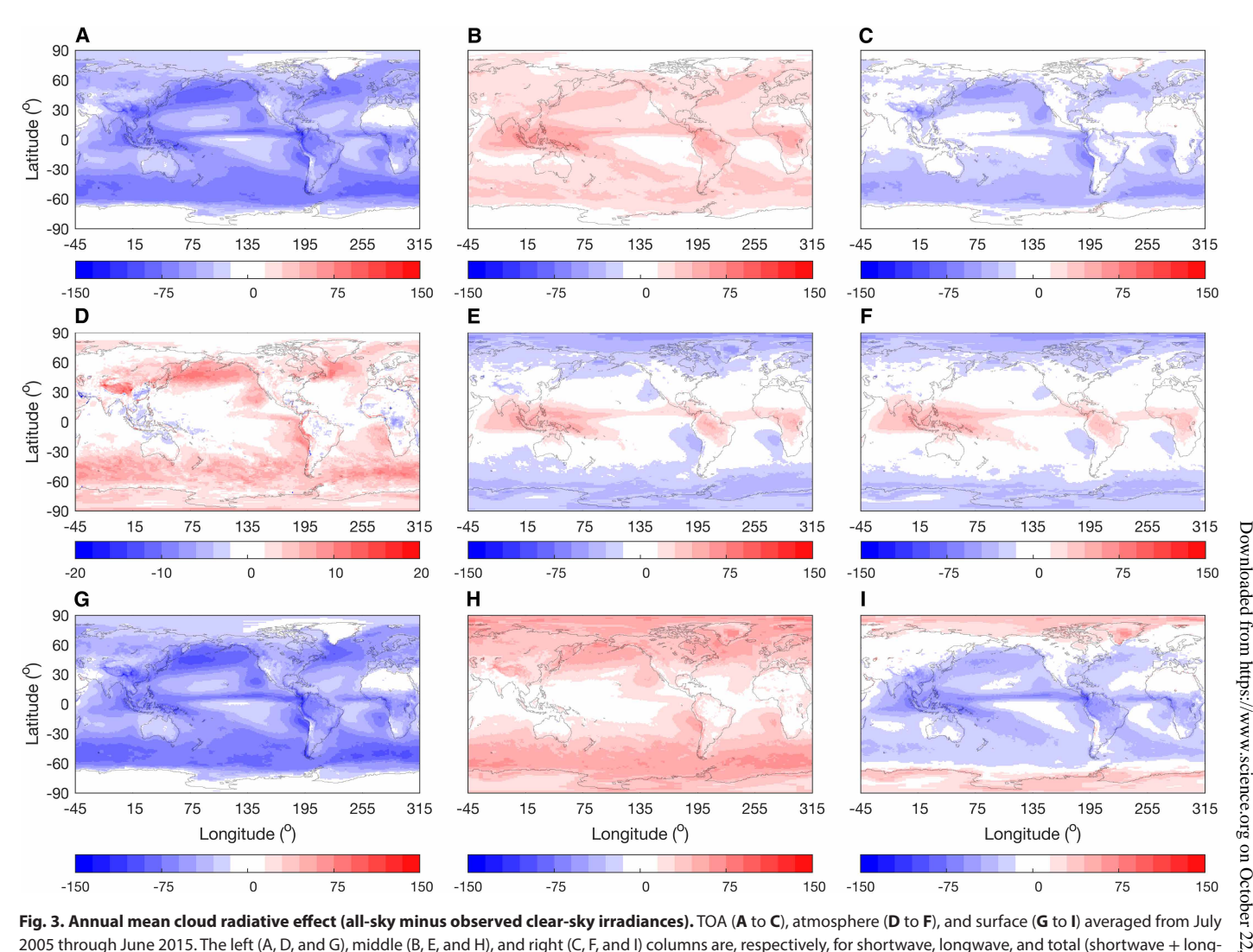


Fig. 3. Annual mean cloud radiative effect (all-sky minus observed clear-sky irradiances). TOA (A to C), atmosphere (D to F), and surface (G to I) averaged from July 2005 through June 2015. The left (A, D, and G), middle (B, E, and H), and right (C, F, and I) columns are, respectively, for shortwave, longwave, and total (shortwave + longwave) irradiances.

As a result, when the surface cloud effect is subtracted from the TOA cloud effect, the cloud effect to the atmosphere is negative over these regions where clouds are lower. When the cloud radiative effect is averaged over the globe, the meridional positive and negative effects partially cancel (34), which leads to a smaller global mean atmospheric longwave cloud radiative effect. In addition, high- and low-level cloud radiative effects to the atmosphere partly cancel (33, 35).

Another way to understand the global mean longwave cloud radiative effect to the atmosphere is that cloud tops are cooled by emission to space and cloud bases are warmed by emission from the surface. In the tropics, clouds reduce atmospheric cooling because of their lower effective cloud top temperature than the effective temperature of water vapor present at lower altitudes. In polar regions, cooling in the atmosphere is enhanced by clouds by increasing emissivity of the atmosphere from clear-sky conditions in which water vapor amount is small. Meridional gradient of longwave cloud effects to the atmosphere, positive TOA cloud effects in the tropics, and negative cloud effects in polar regions are apparent in Fig. 4A.

In summary, the global mean net atmospheric total irradiance trend derived from ~18 years of Clouds and the Earth's Radiant Energy System (CERES) data is slightly negative because a positive trend in net atmospheric shortwave and a negative trend in net atmospheric longwave nearly cancel. Because cloud effects to the net atmospheric irradiances are small, drivers of the trend appear to be clear-sky variables that affect net atmospheric shortwave irradiance, namely, temperature, water vapor, and aerosols. This interpretation is, however, incomplete and does not explain changes in net atmospheric irradiance for months with a large temperature perturbation within the 18-year time period. Results of the attribution analysis by the PRP discussed in the third and fourth subsections of the result section reveal that the importance of longwave changes increases with the magnitude of temperature perturbations.

Evaluation of surface irradiance

To understand the uncertainty in trends, we evaluate Energy Balanced and Filled (EBAF) 4.2.1 computed surface irradiance monthly anomalies with surface observations taken at 42 and 19 ocean

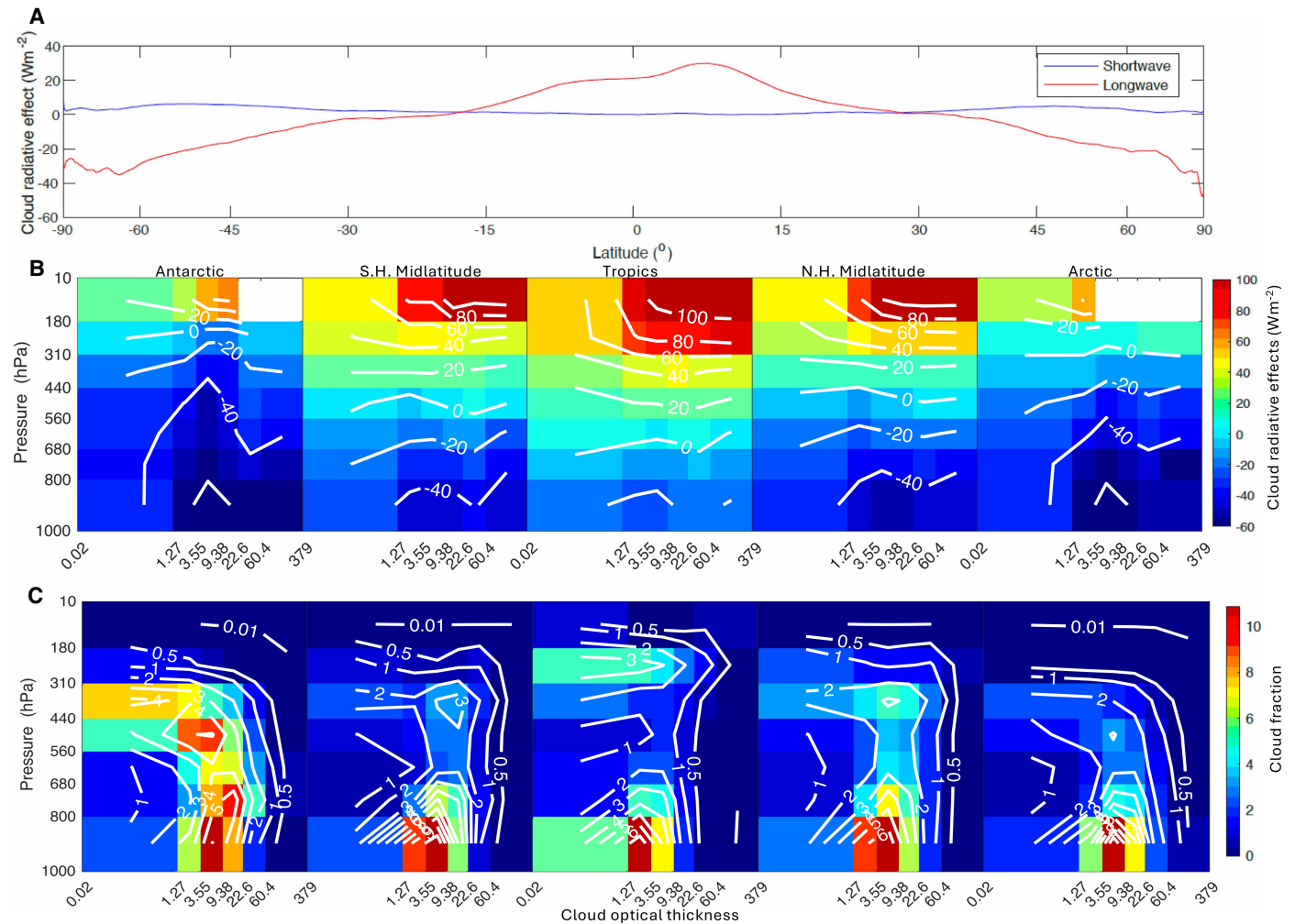


Fig. 4. Mean cloud radiative effects and cloud fraction by cloud type. (**A**) Zonal cloud radiative effects to the atmosphere for shortwave (blue line) and longwave (red line), (**B**) daily mean shortwave + longwave atmospheric cloud radiative effects by single layer clouds in watts per square meter (Wm⁻²) derived from January, April, July, and October 2018 Edition 4 CRS data product as a function of cloud optical thickness and cloud top pressure for, left to right, Antarctica (90°S to 60°S), Southern Hemisphere (S.H.) mid-latitude (60°S to 30°S), tropics (30°S to 30°N), Northern Hemisphere (N.H.) mid-latitude (30°N to 60°N), and Arctic (60°N to 90°N), and (**C**) 2D histogram of cloud fraction as a function of cloud optical thickness and cloud top pressure derived from the Edition 4A flux by cloud type data product. [(A) and (C)] Plot mean values from July 2005 through June 2015.

buoys for, respectively, downward shortwave and longwave irradiances and 30 land sites for both longwave and shortwave (Fig. 5). We only evaluate downward irradiances here because upward irradiances measured at a land site may not represent a larger area due to inhomogeneous land surfaces. In addition, ocean albedo and emissivity are evaluated in earlier studies [e.g., (36–38)].

When we compute the difference of time series (EBAF – observed), there is around a $\pm 1~\rm Wm^{-2}$ variation in EBAF minus observed anomalies averaged over the sites. Anomaly time series root mean square differences are 0.50 Wm⁻² for downward shortwave and 0.44 Wm⁻² for downward longwave, while the SD of the corresponding EBAF anomaly time series are 0.74 and 1.37 Wm⁻², respectively. The correlation coefficient is 0.82 for downward shortwave and 0.93 for downward longwave irradiance anomalies. Relative to the observations, EBAF displays increasing in downward shortwave (0.10 \pm 0.14 Wm dec⁻¹) and decreasing in downward longwave (–0.05 \pm 0.15 Wm⁻² dec⁻¹). Ocean and land separate values are shown in

table S1. While the difference of downward longwave irradiance anomalies over ocean plus land is not significant, when land and ocean are separated, the difference is statistically significant. The reason for the statistically significant difference is unknown. Assuming that uncertainties in the EBAF and observed anomaly trends are equally contributing to the trend differences shown in Fig. 5 (B and D), we consider $0.17 \, \mathrm{Wm}^{-2} \, \mathrm{dec}^{-1} \, [(0.10^2 + 0.14^2 + 0.05^2 + 0.15^2)/2]^{1/2}$ as a plausible uncertainty of atmospheric net total irradiance trend in addition to 5 to 95% confidence intervals. Because computed irradiances are adjusted to match observed TOA irradiances (2, 39), computed TOA irradiance anomaly time series agrees with observed TOA irradiance anomaly time series (2, 39).

Contributions to net irradiance trends

The PRP allows us to separate atmospheric irradiance trends into contributions from atmospheric and surface properties, aerosol (hereinafter clear-sky variables) and cloud. Those atmospheric,

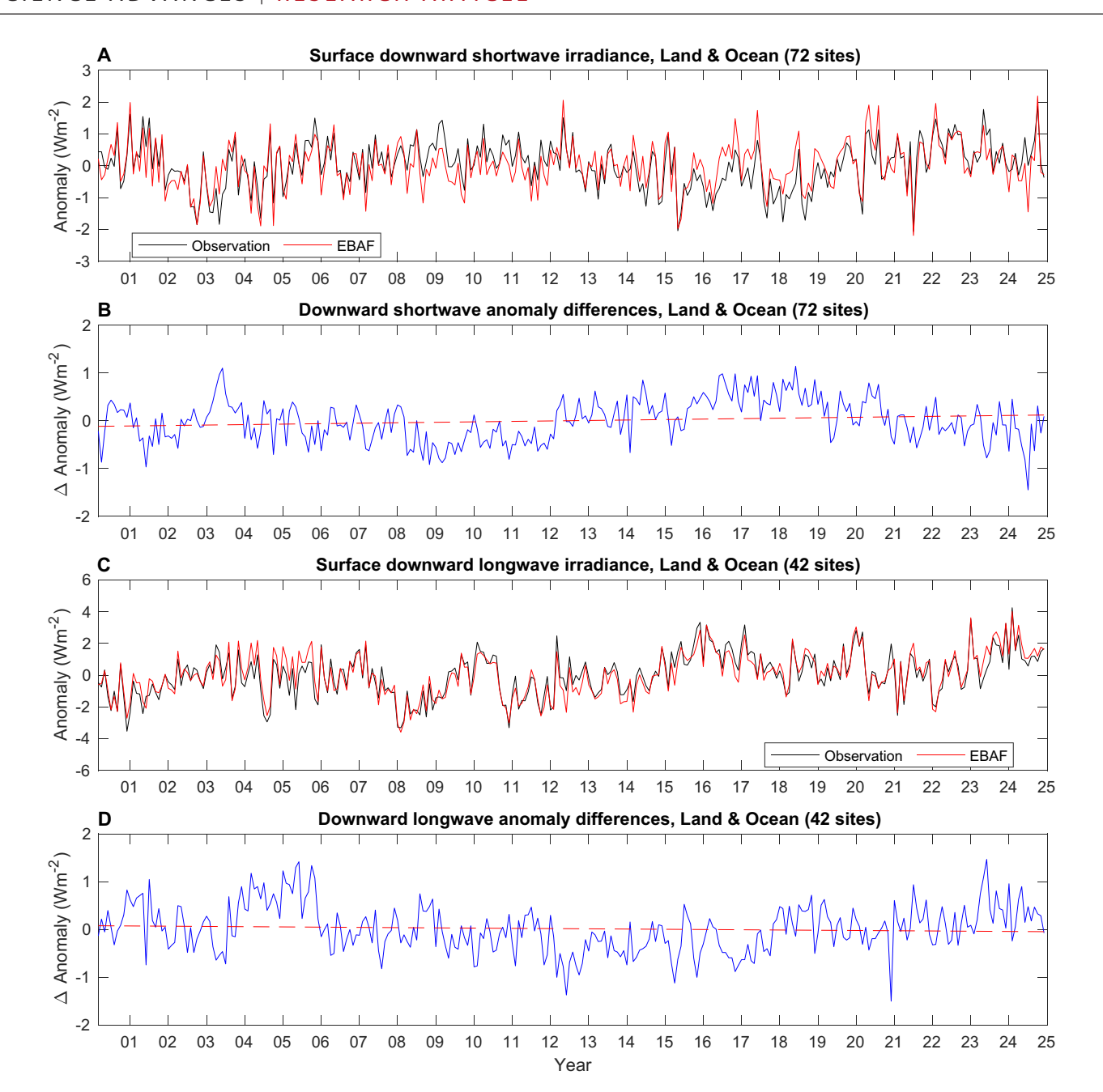


Fig. 5. Monthly anomaly time series of observed and computed surface downward irradiances. (A) shortwave over 72 surface sites (42 ocean buoys and 30 land sites) and (C) downward longwave over 42 surface sites (42 ocean buoys and 30 land sites). Black lines are computed using observations by the method described by Kato et al. (25). Red lines are corresponding Edition 4.2.1 EBAF irradiances anomalies. Differences of anomaly time series (computed minus observed) are shown in (B) for downward shortwave and (D) for downward longwave irradiances. Red dashed lines are linear regression lines. The slope and 5 to 95% confidence intervals of the regression line are $0.10 \pm 0.14 \, \text{Wm dec}^{-1}$ for downward shortwave and $-0.05 \pm 0.15 \, \text{Wm}^{-2}$ dec⁻¹ for downward longwave irradiance anomaly differences.

surface, cloud, and aerosol properties are used in surface irradiance computations.

Figure 6 shows clear-sky variables' and cloud's contributions to net atmospheric shortwave, longwave, and total irradiance trends. The uncertainty of the trends, which is shown by the gray lines is computed by

$$\sigma_x = \left(\Delta F_x^2 + \sigma_{\text{trend},x}^2\right)^{\frac{1}{2}} \tag{1}$$

where ΔF is the difference between the trend derived from the EBAF product and the sum of all PRP trends (total), σ_{trend} is the 5 to 95% confidence interval of the EBAF slope, and subscript x is the net shortwave, net longwave, or net total irradiance. As shown in Fig. 6, the uncertainty σ_x is smaller than larger contributions we discuss in this section. In addition, the envelope of σ_x does not overlap with 5 to 95% confidence intervals of trends of large contributors (e.g., water vapor, air temperature, and skin temperature).

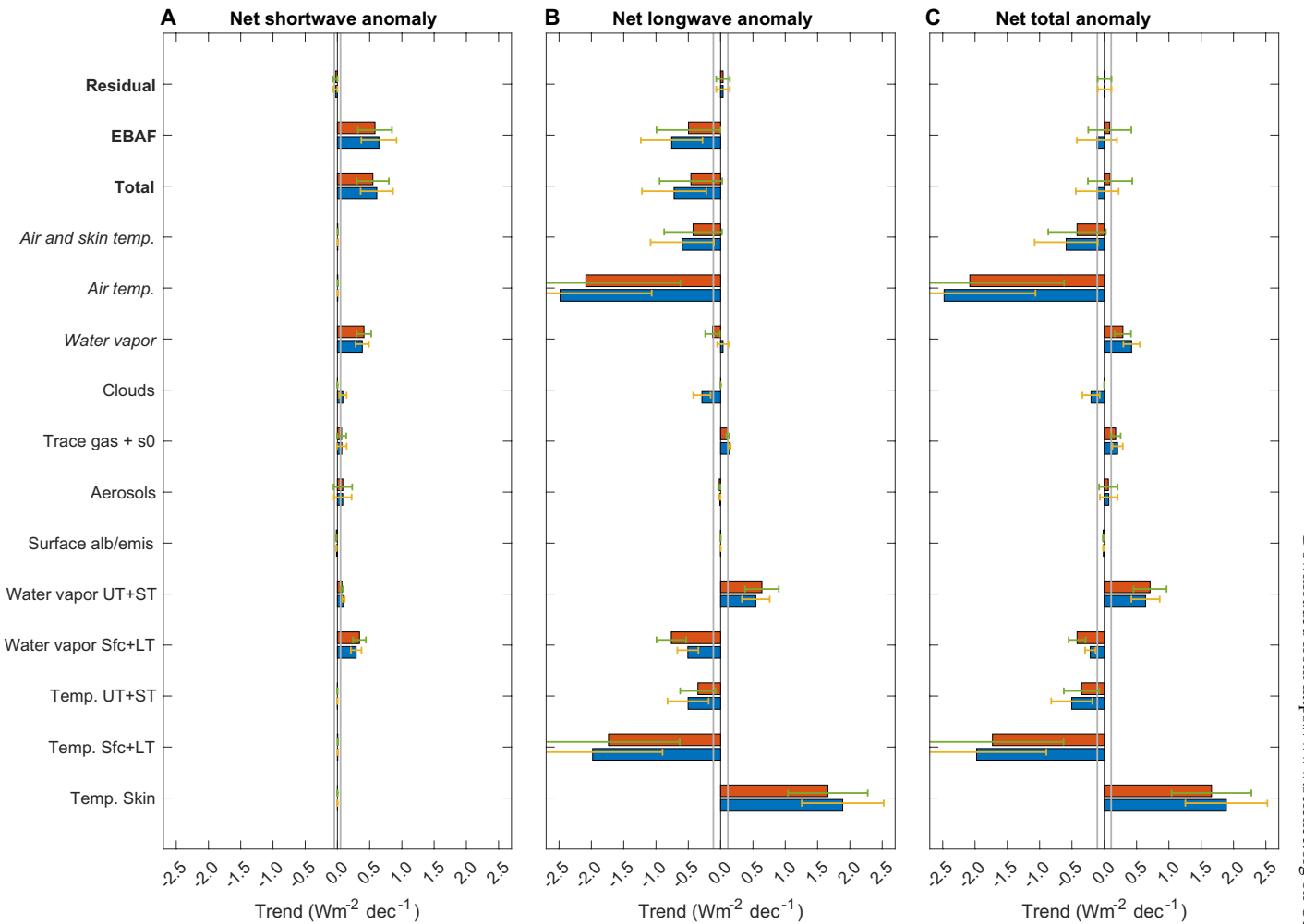


Fig. 6. Contributions by atmospheric and surface property and cloud changes to global net irradiance trends. (A) net shortwave, (B) net longwave, and (C) net total atmospheric irradiance trends for the time period from April 2006 through December 2024. Sfc, LT, UT, ST, and S0 indicate, respectively, surface, lower troposphere (pressure \geq 500 hPa), upper troposphere (500 hPa > pressure \geq 200 hPa), stratosphere (pressure < 200 hPa), and solar constant. The trend labeled "total" is the sum of all contributions indicated by a non-italic font, and the trend labeled "EBAF" is the trend derived from the Edition 4.2.1 EBAF product. Residual is the difference of total and EBAF trends. Blue bars are for all-sky, and red bars are for clear-sky. The numbers in the plots indicate trends in watts per square meter per decade (Wm $^{-2}$ dec $^{-1}$). Error bars indicate 5 to 95% confidence intervals of trends equally extending on both sides, and vertical gray lines are uncertainty computed by Eq. 1.

Increasing water vapor in the atmosphere, especially in the lower troposphere, contributes most toward increasing shortwave absorption in the atmosphere. Increasing water vapor in the lower troposphere also increases longwave cooling in the atmosphere. Although the magnitude of the longwave cooling is larger than the magnitude of the warming by shortwave absorption by water vapor, the longwave cooling increase caused by increasing water vapor in the lower atmosphere is mostly offset by increasing water vapor in the upper troposphere. The net effect of the water vapor increase to the net atmospheric longwave irradiance trend is slightly negative (i.e., increased longwave cooling), $-0.04 \pm 0.09 \text{ Wm}^{-2} \text{ dec}^{-1}$ for all-sky and $-0.12 \pm 0.09 \text{ Wm}^{-2} \text{dec}^{-1}$ for clear-sky (table S2). When both shortwave and longwave effects are added, because the shortwave heating is larger than longwave cooling, the effect of water vapor increase in the atmosphere to the net atmospheric total irradiance trend is positive, $0.42 \pm 0.13~\mathrm{Wm}^{-2}~\mathrm{dec}^{-1}$ for all-sky and $0.29 \pm 0.12~\mathrm{Wm}^{-2}$

 dec^{-1} for clear-sky (Fig. 6 and table S2). The net atmospheric longwave irradiance is also affected by temperature change. Increasing air temperature increases emission by the atmosphere, while increasing skin temperature increases absorption of radiation in the atmosphere emitted by the surface. The net effect of the skin and air temperature changes to the net atmospheric longwave irradiance change is, therefore, smaller than the individual component contributions -0.59 ± 0.45 Wm⁻² dec⁻¹ for all-sky and -0.43 ± 0.23 for clear-sky (table S2).

We revisit Fig. 2 in light of the results of the attribution analysis. The trend of the net atmospheric total irradiance is a result of partially canceled contributions from skin temperature, air temperature, and water vapor to the net atmospheric longwave irradiance and a positive trend of the net atmospheric shortwave irradiance due to increasing absorption in the atmosphere. In the following sections, we further investigate how these balances change when temperature perturbations are large.

Contributions to monthly anomalies

To investigate how individual contributions partially cancel and the net atmospheric shortwave trend offsets the net atmospheric long-wave trends during the time period, we investigate anomaly time series of contributions in this section. In addition, investigating time series allows us to understand how contributions change depending on the size of anomalies and natural variability. Furthermore, using months with larger anomalies of temperature and water vapor amount, we can understand how their contributions to the net atmospheric longwave irradiance changes compared to water vapor contribution to the net atmospheric shortwave irradiance.

Before we investigate contributions, we evaluate the agreement between the time series of net atmospheric total irradiance anomalies and the sum of all contributions to net atmospheric total irradiance anomalies (Fig. 6, top plot). The agreement of the two lines is good: The correlation coefficient is 0.93, and square mean difference is 14% of the variance of EBAF net atmospheric total irradiance anomalies of 0.45 (Wm⁻²)².

To understand how shortwave and longwave trends nearly cancel, Fig. 7 also shows time series of temperature, water vapor, and surface albedo + aerosol contributions to net atmospheric longwave and shortwave irradiances. Negative contributions of increasing

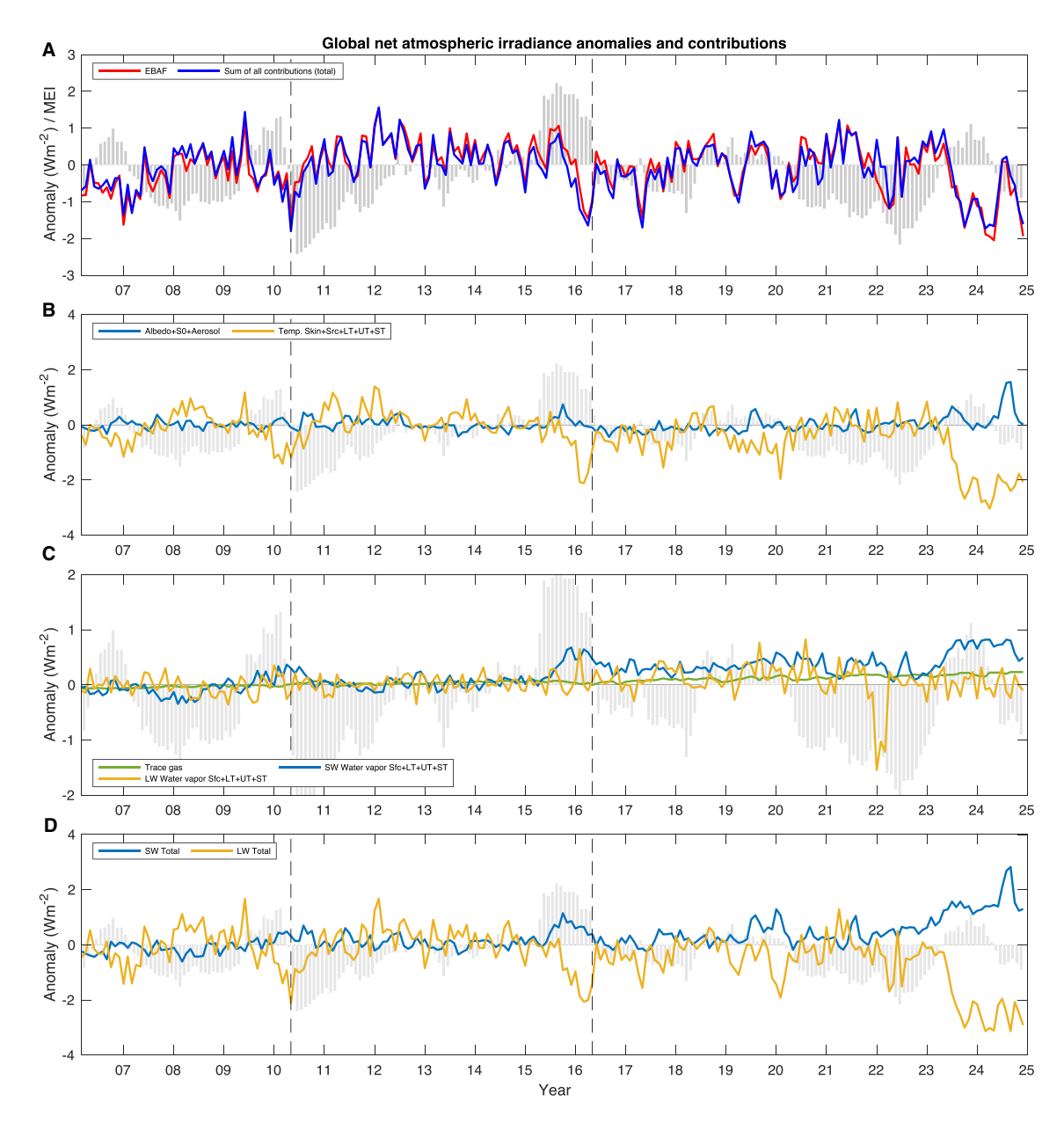


Fig. 7. Monthly anomaly time series of irradiance anomalies and contributions. (A) EBAF atmospheric total irradiances (red line) and the sum of all contributions (blue line). The vertical dashed lines indicate three periods based on ENSO index used by Loeb et al. (42), April 2006 through May 2010, June 2010 through May 2016, and June 2016 through December 2024. Shaded bars indicate multivariate ENSO index (MEI) (71). (B to D) Contributions from surface albedo + solar constant (S0) + aerosol, temperatures, water vapor, and trace gases to global net atmospheric shortwave (SW, blue lines) and longwave (LW, orange lines) irradiance anomalies. Sfc, LT, UT, and ST indicate, respectively, surface, lower troposphere (pressure ≥ 500 hPa), upper troposphere (500 hPa > pressure ≥ 200 hPa), and stratosphere (pressure < 200 hPa).

temperature to the longwave irradiance anomalies and positive contributions of increasing water vapor to the shortwave anomalies are apparent. Larger aerosol contributions in 2024 appear to be due to fires in the Amazon [e.g., (40)].

To understand partial cancelations among contributions to longwave, we further partition temperature and water vapor contributions to the longwave anomalies into surface and lower troposphere, upper troposphere, and stratosphere. When these components are separated, larger anomalies are clearly apparent (fig. S2). Figure S2 also highlights cancelations of larger contributions to longwave anomalies especially after ~2016. Specifically, anticorrelations between the air temperature and surface skin temperature contributions are apparent; the correlation coefficient is -0.92. Similarly, anticorrelations between the surface and lower troposphere (Sfc + LT) water vapor and upper troposphere and stratosphere (UT + ST) are also apparent, consistent with Previdi (41), with a correlation coefficient of -0.80.

When the entire time series is separated into three subsections depending on El Niño-Southern Oscillation (ENSO) phase used in Loeb *et al.* (42), larger perturbations of temperature and water vapor that lead to larger contributions to longwave are apparent in the third

period from June 2016 to December 2023 (Fig. 7 and fig. S2). Partial cancelations of these contributions also occur in the third period when perturbations are large. Larger monthly anomalies also occur, for example, in May 2010, April 2016, and October 2023. Negative contributions of upper troposphere and stratosphere (UT + ST) water vapor to net atmospheric longwave irradiance anomalies in early 2022 appear to be associated with large water vapor anomalies in UT + ST caused by Hunga Tonga eruption, which occurred in December 2021 (43–45).

To investigate how net atmospheric shortwave and longwave anomalies change when perturbations are large, we select three months, May 2010, April 2016, and October 2023. All three months occur during or right after El Nino events and exhibit larger negative anomalies of global monthly net atmospheric total irradiance. Figure 8 shows contributions from atmospheric and surface variables to shortwave, longwave, and total net atmospheric irradiance anomalies for these three months. Unlike trend contributions in the overall time series, contributions to the net atmospheric total irradiance anomalies are dominated by longwave components in these months. Although regional patterns of water vapor, air temperature, and surface

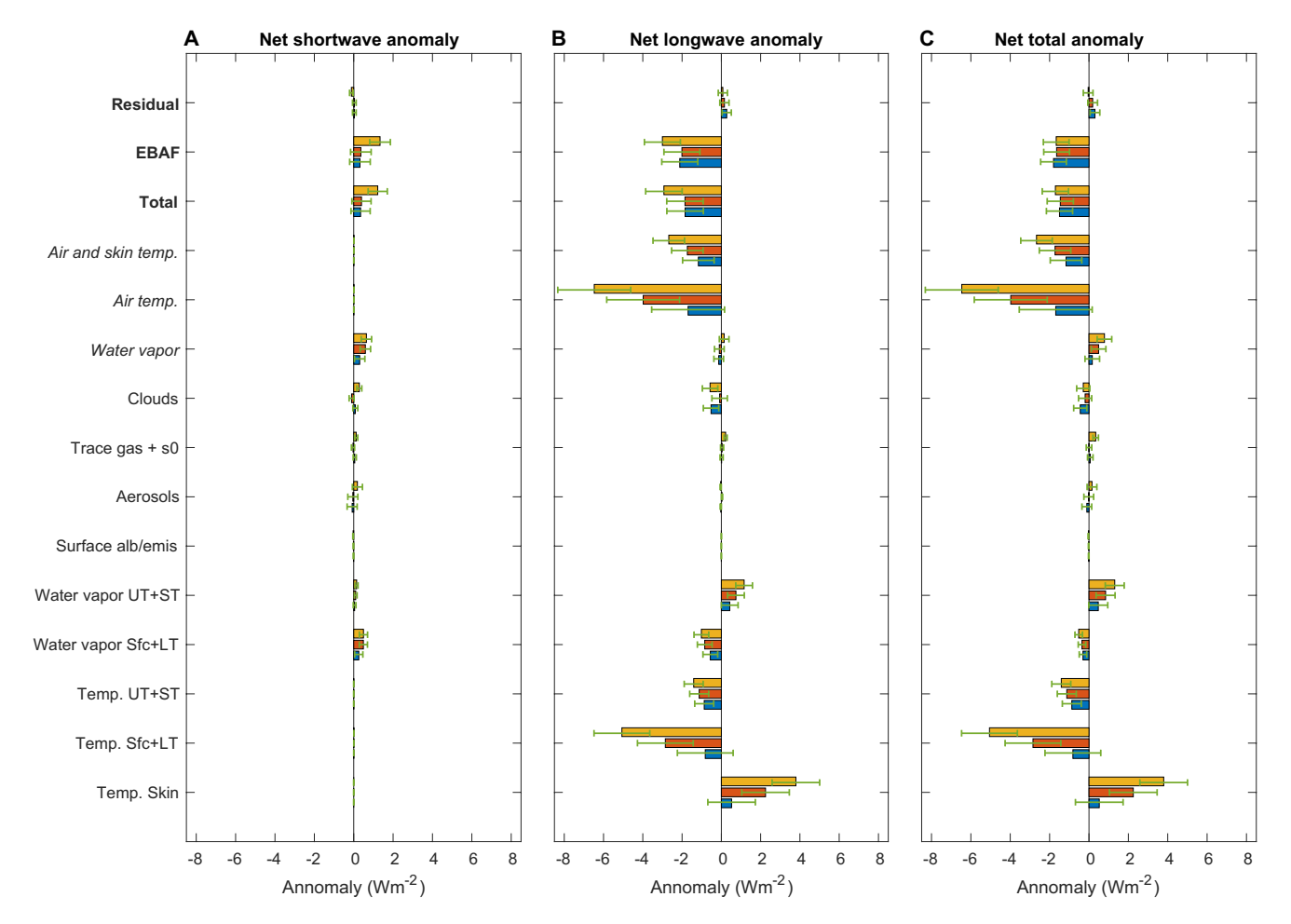


Fig. 8. Contributions by atmospheric and surface property changes to net irradiance anomalies. (A) net shortwave, (B) net longwave, and (C) net total atmospheric irradiance anomalies for May 2010 (blue), April 2016 (red), and October 2023 (orange). Sfc, LT, UT, ST, and s0 indicate, respectively, surface, lower troposphere (pressure ≥ 500 hPa), upper troposphere (500 hPa > pressure ≥ 200 hPa), stratosphere (pressure < 200 hPa), and solar constant. The anomaly labeled total is the sum of all contributions from variables written in a non-italic font, and the anomaly labeled EBAF is the anomaly derived from the Edition 4.2.1 EBAF product. Residual is the difference of total and EBAF anomalies. Error bars indicate the SD of global monthly anomalies and contributions.

skin temperature anomalies differ for these three months (fig. S3), signs of their contributions to longwave net atmospheric irradiance anomalies are the same. Larger anomalies of water vapor, air temperature, and skin temperature lead to their larger contributions. Contributions of water vapor in the surface and lower troposphere and in the upper troposphere and stratosphere nearly cancel each other. Therefore, the net atmospheric longwave anomalies are driven by temperature anomalies, which are elevated by the El Nino warming conditions. Contributions of air temperature in the atmosphere to the net atmospheric longwave are larger than skin temperature contributions so that the net atmospheric longwave anomalies are negative (more cooling). Water vapor contributions to net shortwave anomalies are substantial for these months. However, the magnitude of the negative net atmospheric longwave irradiance anomalies is larger than the positive anomalies of the net atmospheric shortwave irradiance, which leads to negative net atmospheric total irradiance anomalies.

Global net atmospheric total irradiance trend compared with trend of diabatic heating by precipitation

Because global precipitation is strongly constrained by net atmospheric radiative cooling, we attempt to reconcile these key climate

variables, which is of fundamental importance to understanding the influence of climate change on the global water cycle. We compare time series of global net atmospheric total irradiance anomalies with other energy flux component anomalies that contribute to atmospheric energy budget. When we consider energy budget change in the atmosphere, the global mean atmosphere energy balance is (46, 47)

$$\Delta F_{\text{net,rad}}^{\text{atm}} + \Delta J_{\text{precip}} - \Delta F_{\text{SH}} = \Delta \left(D \dot{S} E + \dot{K} E \right)$$
 (2)

where $\Delta F_{\rm net,rad}^{\rm atm}$ is the net atmospheric total irradiance change, $\Delta J_{\rm precip}$ is the change of diabatic heating by precipitation, $\Delta F_{\rm SH}$ is the sensible heat flux change (positive downward, hence the minus sign in front of it), and Δ (DSE+KE) is the change of the dry static and kinetic energy storage rate in the atmosphere. At a global and annual scale, the storage term on the right side is small compared to the terms on the left side so that three energy components on the left side balance.

To test the balance of anomalies, Fig. 9A shows global mean anomaly time series of diabatic heating by precipitation, net atmospheric total irradiance, surface sensible heat flux, and dry static and kinetic energy tendencies. Monthly anomalies are smoothed by a

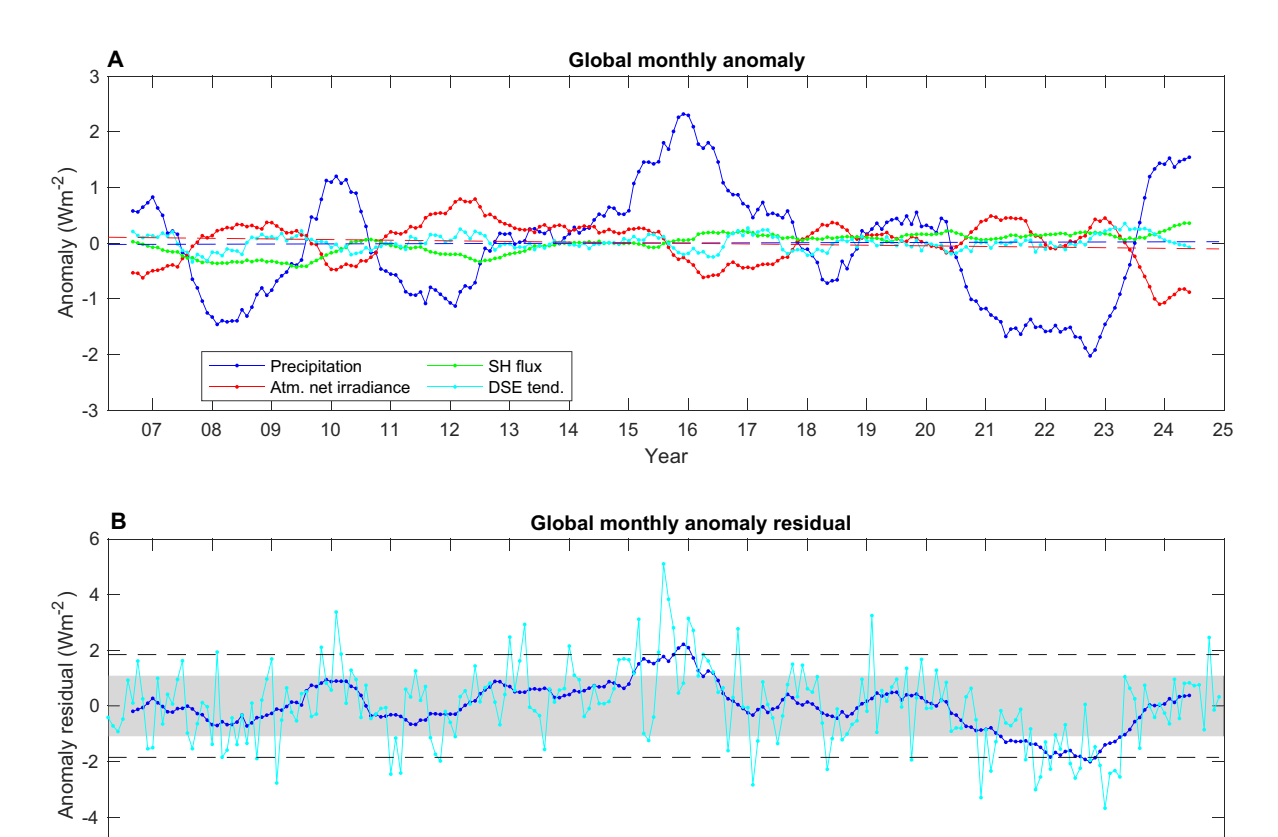


Fig. 9. Anomaly time series of energy flux and balance residual. (A) Anomaly time series of (blue) precipitation, atmospheric net total irradiance (red), surface sensible heat flux (green), and dry static and kinetic energy tendency (cyan). Monthly anomalies are smoothed with a 12-month moving window. Blue and red dashed lines are linear regression lines of the precipitation and irradiance time series, respectively. (B) Anomaly time series of the sum of four energy components shown in (A). Blue and cyan lines are with and without using a 12-month moving window. Shade area and dashed lines are plus minus of the square root of the sum of four energy component anomaly variances computed with and without a 12-month moving window, respectively.

15

16

Year

18

19

20

21

24

-6

07

08

09

10

12

13

14

12-month moving window. Although there are large differences in their magnitudes, anomalies of net atmospheric total irradiances and diabatic heating by precipitation are anticorrelated. To understand how atmospheric energy budget anomalies are balanced, we define anomaly residual ϵ as

$$\varepsilon = \Delta F_{\text{net,rad}}^{\text{atm}} + \Delta J_{\text{precip}} - \Delta F_{\text{SH}} - \Delta \left(\dot{\text{DSE}} + \dot{\text{KE}} \right)$$
 (3)

The time series of the residual is shown in Fig. 9B. To understand how well these components are balanced, we assume that all fluxes are independent and compute the square root of the sum of variances of anomalies computed with and without the 12-month smoothing

$$\sigma^2 = \sigma_{\text{atm pet rad}}^2 + \sigma_{\text{precip}}^2 + \sigma_{\text{SH}}^2 + \sigma_{\text{DSE KE}}^2$$
 (4)

where $\pm \sigma$ with the smoothing is indicated by the shade and $\pm \sigma$ without the smoothing is indicated by the dashed lines. When the anomaly time series is within the corresponding $\pm \sigma$ envelope, errors are correlated or they are smaller for these months. A substantial part of the time series is within the envelopes; 82% of 213 months shown by the cyan line in Fig. 9B is within $\pm \sigma$ shown by the dashed lines. For the smoothed anomalies, time periods around 2016 and 2023 are outside the envelope. Larger precipitation rates around 2016 appear to be caused by larger precipitation anomalies associated with El Nino events in which the global distribution of precipitation is altered with more precipitation over the ocean relative to the land. Likewise, large negative precipitation anomalies from 2021 to 2023 are associated with La Nina events. These anomalies and anomalies in general depend on data products because precipitation biases depend on observing system, resolutions, and samplings, as well as assumptions in algorithms (48).

Anomalies of net atmospheric total irradiance and diabatic heating by precipitation are fitted (Fig. 9A), and the slopes of the linear regression line are summarized in Fig. 10. The trend of net atmospheric total irradiance is 0.11 \pm 0.31 Wm^{-2} , and the trend of diabatic heating by precipitation is 0.03 \pm 0.61 Wm^{-2} (corresponds to 0.001 \pm 0.021 mm

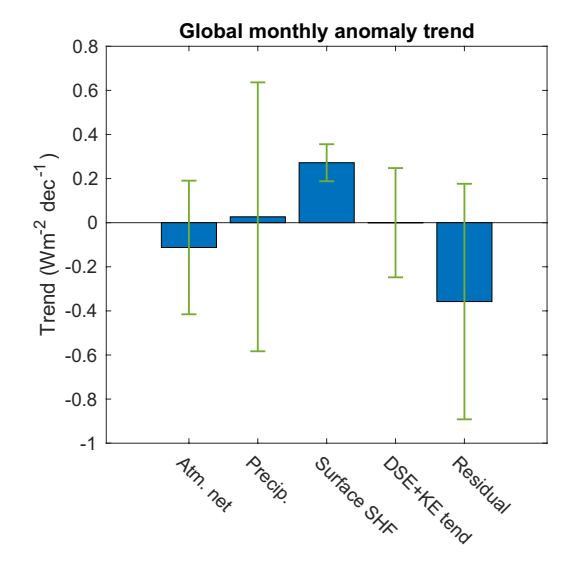


Fig. 10. Summary of trends of global monthly anomalies for the period from April 2006 through December 2024. Error bars indicate 5 to 95% confidence intervals.

day⁻¹ dec⁻¹). Both trends in the past 18 years are not statistically significant. An estimate of uncertainty in the net atmospheric total irradiance derived using surface observation is 0.17 Wm⁻² dec⁻¹ (see the first subsection of the Results section). Therefore, the magnitude of the trends of net atmospheric total irradiance and diabatic heating by precipitation agree to within the uncertainty of net atmospheric total irradiance trend.

Despite the agreement between net atmospheric total irradiance trend and diabatic heating by precipitation, a closure of the atmospheric energy anomaly trend has not been achieved. A negative trend of the residual indicates that the residual is more negative toward the end of the time series. The residual trend is driven by the trend of sensible heat flux anomalies. Note that the positive trend of sensible heat flux anomalies contributes as a negative trend in the residual because of the negative sign in front of $\Delta F_{\rm SH}$ in Eq. 3; increasing the downward positive $F_{\rm SF}$ is energy loss for the atmosphere. Therefore, the trend of the residual is mostly driven by the trend of sensible heat flux anomalies. Whether a large trend of sensible heat flux anomalies is real or artifacts is unknown. However, the result shows that the trend of the global mean diabatic heating rate by precipitation is not affected by the larger trend of the sensible heat flux.

DISCUSSION

We have provided observational evidence that a lack of significant trends in global mean precipitation since 2006 is consistent with nearly constant (e.g., statistically insignificant) net radiative cooling and explained by compensation between increasing longwave cooling due mostly to increasing temperature and increasing shortwave heating due to increasing water vapor. Increasing water vapor increases global mean shortwave absorption in the atmosphere. Increasing surface and lower tropospheric water vapor increases cooling from the atmosphere and emission primarily to the surface, which is nearly offset by warming caused by increasing water vapor in upper troposphere and stratosphere as suggested previously based on theoretical calculations (41). Increasing air temperature and skin temperature cause, respectively, cooling and warming effects to the atmosphere. Because air temperature and skin temperature contributions to the longwave trend nearly cancel out, the longwave contribution to the net atmospheric total irradiance is nearly equal to the contribution by increasing shortwave absorption caused by increasing water vapor.

When we look at individual months, contributions from temperature and water vapor anomalies to the net atmospheric longwave irradiance anomalies are larger than their contributions to the net atmospheric shortwave irradiance anomalies. Larger anomalies in near surface and lower tropospheric air temperature can lead to increasing longwave cooling in the atmosphere. A larger temperature contribution to increase atmospheric cooling makes the longwave cooling change much larger than increasing shortwave absorption by increasing water vapor. Although the net atmospheric total irradiance trend is nearly constant in the past ~18 years, this result implies that if larger temperature and water vapor anomalies persist and temperature continues increasing, atmospheric cooling will increase, exceeding shortwave absorption and leading to a negative trend of the net atmospheric total irradiance. A brief period of persistent warm temperature from 2023 to 2024 could be a glimpse into future changes in which radiative cooling increases with an increase of temperature, as shown in modeling studies. This result also implies that the global mean net atmospheric total irradiance may not change linearly with increasing surface temperature during time periods when temperature perturbations are not very large. Therefore, this result explains a statistically insignificant precipitation trend and the difficulty of observing global mean precipitation trend when warming caused by radiative forcing is not large (21), which is compounded by the difficulty in accurately observing long-term changes in global mean precipitation.

The result of the study of Loeb *et al.* (27) shows that the contribution of water vapor to the net TOA shortwave trend is less than 0.1 Wm⁻² dec⁻¹, while net TOA shortwave trend is 0.65 Wm⁻² dec⁻¹. However, the trend of shortwave absorption in the atmosphere is 0.31 Wm⁻² dec⁻¹ for all-sky and 0.33 Wm⁻² dec⁻¹ for total area clear-sky for the same period (September 2002 through March 2020), which is primarily caused by increasing water vapor in the atmosphere. The water vapor increase in the atmosphere reduces shortwave absorption by the surface (ocean) and increases shortwave absorption in the atmosphere by nearly the same amount.

Annual global mean TOA total irradiance variability and the variability of ocean heating rates derived from in situ observations agree very well (27). Our results indicate that increasing water vapor amount in the atmosphere substantially increases shortwave absorption in the atmosphere, a substantial warming influence that has been previously identified in regions to reduced surface solar irradiance [e.g., (49)]. To understand the consistency of our results with earlier studies, we need to consider other energy flux components contributing to atmosphere and surface energy budget changes.

Because there is a strong balance between net atmospheric radiative cooling and diabatic heating by precipitation constrained by physical grounds [e.g., (21)], the change in $\Delta F_{\rm net,rad}^{\rm atm}$ has implications for global water cycle changes. We identify that both $\Delta F_{\rm net,rad}^{\rm atm}$ and $\Delta J_{\rm precip}$ had no statistically significant trends in the past ~18 years. If we express net energy flux change at the surface, $\Delta F_{\rm net}^{\rm sfc}$, the global mean surface energy balance is

$$\Delta F_{\rm net}^{\rm sfc} = \Delta F_{\rm net,rad}^{\rm sfc} + \Delta F_{\rm LH} + \Delta F_{\rm SH} = \Delta F_{\it net,rad}^{\rm TOA} - \Delta \left(\dot{\rm MSE} + \dot{\rm KE} \right) \ \, (5)$$

where $\Delta F_{\rm net,rad}^{\rm sfc}$ is the net surface total irradiance change, $\Delta F_{\rm LH}$ is the latent heat flux change (positive downward), $\Delta F_{\rm net,rad}^{\rm TOA}$ is the net TOA total irradiance change, and Δ (MŚE+KĖ) is the change in the moist static and kinetic energy storage rate in the atmosphere. Loeb *et al.* (27) show that $\Delta F_{\rm net,rad}^{\rm TOA}$ is increasing. Energy is deposited to warm the climate system at a rate of 0.5 Wm $^{-2}$ dec $^{-1}$. Von Schuckmann *et al.* (50) show that 89% of the energy stored in the climate system is used for heating ocean, 5% for heating land, 4% for heating cryosphere, and 2% for heating atmosphere over the period 2006–2020. Therefore, 99% of $\Delta F_{\rm net,rad}^{\rm TOA}$ is used for $\Delta F_{\rm sfc}^{\rm Sc}$ and 1% is used for Δ MSE. The trend of global monthly mean MSE tendency derived from ERA5 is 0.01 Wm $^{-2}$ dec $^{-1}$.

Energy equation of water is

$$\Delta M\dot{S}E - \Delta D\dot{S}E = \Delta F_{LH} - \Delta J_{precip}$$
 (6)

Equation 6 can be derived from Eqs. 2 and 5, and $\Delta F_{\rm net}^{\rm TOA} = \Delta F_{\rm net}^{\rm atm} + \Delta F_{\rm net}^{\rm sfc}$. Increasing water vapor in the atmosphere is the result of $\Delta F_{\rm LH} > \Delta J_{\rm precip}$. The trend of global monthly mean DSE storage rate derived from ERA5 is slightly less than the trend of MSE storage rate, consistent with increasing water vapor in the atmosphere. This study

investigates the relationship described by Eq. 2, while TOA net irradiance change uses the relationship expressed by Eq. 5. This study observationally confirms that precipitation trend in the past ~18 years is constrained by net atmospheric total irradiance trend.

Although global annual mean energy of the atmosphere has a residual of about 10 Wm⁻² when observation-based data products are used [e.g., (46, 51)], results of this study show that anomalies of flux components derived from observations and the size of net atmospheric irradiance and diabatic heating by precipitation trends derived from them are reasonably consistent. This implies that the residual is approximately constant with time. As discussed in this section, our results are also consistent with earlier studies' investigating Earth energy budget using observations. While observations of energy components need to be further improved to establish a better balance of anomalies, the agreement shown in this study is encouraging especially considering that data products used in this study were developed independently. One caveat is that uncertainties of the trends used in this study are mostly statistical uncertainty. We only considered the trend uncertainty of 0.17 Wm⁻² dec⁻¹ estimated using surface observations as a proxy of the trend uncertainty of the net atmospheric total irradiance caused by inputs and assumptions in producing EBAF irradiances. We have not rigorously considered trend uncertainties caused by inputs, and assumptions used in producing the data products are therefore an important priority in future research.

In conclusion, we provided observational evidence that increasing shortwave absorption caused by increasing water vapor substantially contributes to the trend in net atmospheric total irradiance (a reduction in net radiative cooling of the atmosphere). We identified that the shortwave contribution mostly offsets increasing longwave cooling caused by increasing temperature and water vapor. Last, we found that this trend in net atmospheric radiative cooling is physically linked to diabatic heating by precipitation based on independent observing system. Both trends in the past ~18 years are not statistically significant. In addition, the trend of diabatic heating by precipitation agrees to within the uncertainty of net atmospheric total irradiance. We showed that ERA5 surface sensible heat flux has larger trend, although the cause of the trend is unknown. The large surface sensible heat trend does not affect the trend of diabatic heating by precipitation. This agreement provides physical consistency of the result, which has implication for future changes in the global water cycle as climate continues to respond to varying greenhouse gas and aerosol forcing.

MATERIALS AND METHODS

We use the CERES Edition 4.2.1 EBAF product, the version 3.2 GPCP precipitation product, and the ERA5 reanalysis product.

Edition 4.2.1 EBAF TOA and surface irradiances

The CERES project (52) has been producing continuous global TOA and surface irradiance data products with month starting since March 2000. While TOA irradiances are derived directly from satellite radiance observations, surface irradiances are computed using retrieved properties. Issues in deriving the trend of atmospheric net irradiance arise because of artifacts in the inputs used for the computations of surface irradiances. Geostationary satellite–derived cloud properties are used to resolve cloud diurnal cycle (53–55). Because geostationary satellite imagers change when older satellites are replaced by newer satellites, cloud properties derived from geostationary satellites

introduce discontinuities in surface irradiance anomaly time series (25). However, cloud properties derived from two sun-synchronous orbits separated by 3 hours around the local solar noon (e.g., Terra and Aqua) are sufficient to capture cloud diurnal cycles to compute daily and monthly mean irradiances (39). In addition, surface irradiance anomaly time series derived from one sun-synchronous orbit (e.g., NOAA-20) is nearly identical to anomaly time series derived from Terra and Aqua (39). These results lead to developing an approach using only cloud properties derived from sun-synchronous orbits. The approach has eliminated artifacts caused by geostationary satellites and was used to produce the Edition 4.2.1 EBAF product. The Edition 4.2.1 EBAF product uses Terra + Aqua data from July 2002 through March 2024 and NOAA-20-only data from April 2024 onward. NOAA-20 data start from May 2018. Using NOAA-20 data from May 2018 onward does not change the net TOA, net surface, and net atmospheric irradiance anomaly trends.

Details of the algorithms to produce TOA irradiances and surface irradiances are given in, respectively, the studies of Loeb *et al.* (9, 56) and Kato *et al.* (2, 39). Briefly, TOA irradiances are derived from broadband radiance observations taken by CERES instruments on Terra, Aqua, and NOAA-20 satellites. Radiances are converted to irradiances using angular distribution models described by Su *et al.* (57). The global mean TOA net total irradiance over the time period from 2005 through 2015 is constrained by heating rate derived from in situ ocean temperature measurements (9, 27). Surface irradiances are computed using imager-derived cloud properties (58) and aerosol optical thicknesses.

The source of aerosol optical thicknesses is Terra and Aqua moderate resolution imaging spectroradiometer (MODIS) from March 2000 through March 2022 and NOAA-20 visible infrared imaging radiometer suite (VIIRS) from April 2022 onward. For the MODIS period, aerosol optical thicknesses over ocean are derived by the Dark Target algorithm (59), and aerosol optical thicknesses over land are derived by the Dark Target and Deep Blue (60) algorithms. For the VIIRS period, both Dark Target (61) and Deep Blue (62) algorithms are used for ocean and land.

Because of revisions to the Deep Blue and Dark Target aerosol algorithms for VIIRS, aerosol optical thicknesses derived from VI-IRS are significantly different from those derived from Terra and Aqua MODIS. To mitigate the discontinuity in aerosol optical thickness derived by the Deep Blue algorithm in the transition from MO-DIS to VIIRS, we correct VIIRS-derived aerosol optical thicknesses to match those of MODIS using linear regression between Aqua MODIS and NOAA-20 VIIRS aerosol optical thickness data. The regression coefficients are derived separately for the Deep Blue and Dark Target aerosol datasets. The Deep Blue coefficients vary by month, i.e., 12 sets of coefficients, and are derived in each $0.2^{\circ} \times 0.2^{\circ}$ grid using aerosol optical thickness and scattering angle as predictors. The coefficients for the Dark Target data do not depend on time but vary with aerosol optical thickness. The optical thicknesses from 0 to 3.0 are divided into bins with a width of 0.01, and coefficients are derived for each bin separately.

Sea surface and land skin temperatures are from the Goddard Earth Observing System, version 5.4.1 (GEOS-5.4.1) reanalysis product through March 2022 and from MERRA-2 from April 2022 onward. For clear-sky conditions, land skin temperatures are derived from imager radiances. Air temperature and humidity profiles are obtained from the MERRA-2 reanalysis product for the entire time period. Surface irradiances are computed hourly and averaged

monthly and regionally using $1^{\circ} \times 1^{\circ}$ equal area grids (63). Computed regional monthly mean irradiances are subsequently compared with TOA irradiances derived from CERES measurements. The differences are used to derive biases in atmospheric, cloud, and aerosol properties used for the computations. These biases combined with radiative kernels (64) are used to adjust computed regional monthly surface irradiances (2). Observations taken from the NOAA-20–only period (April 2022 onward) are merged with the Terra + Aqua period (April 2006 through March 2022) by the method described in the studies of Loeb *et al.* (56) for TOA irradiances and Kato *et al.* (39) for surface irradiances.

Deriving anomaly time series using surface observations

Because surface observations at a given site are often not continuous throughout the entire period and the total number of sites can change for a given month, we compute the anomaly time series of each site separately and add resulting anomaly time series by the method described by Kato *et al.* (25). Briefly, we first deseasonalize the observed irradiance individual site separately by subtracting the climatological monthly mean of the corresponding calendar month. Second, we normalize the deseasonalized time series by respective SD and add time series from all sites. Third, we multiply the resulting time series by the ratio of the SD of corresponding EBAF anomaly time series to the SD of the combined surface sites anomaly time series.

Precipitation, surface sensible heat, and dry static and kinetic energy tendency data products

We use the GPCP version 3.2 data product (65, 66). We use the GPCP product for this study because it is based on observations and covers global land and ocean. In addition, time series are analyzed in earlier studies (22, 23, 67) and show no significant discontinuities. We use the enthalpy of vaporization at 0°C to convert millimeter per day (mm day⁻¹) to watts per square meter (Wm⁻²). The error caused by ignoring temperature dependence of the enthalpy of vaporization and assuming all liquid phase precipitation in a global mean value is less than 1 Wm⁻² (68). The associated error in the anomalies is even smaller. Surface sensible heat fluxes and dry static and kinetic energy tendencies are from ERA5. Tendencies are derived by the method described by Mayer *et al.* (51).

Partial radiative perturbation

We use the PRP method (69) to quantify contributions to atmospheric irradiance trends. The algorithm is explained by Thorsen et al. (64) and used in a study by Loeb et al. (27). The algorithm is based on wide two-sided PRP calculations. Centered TOA, surface, and atmospheric irradiance differences δF are computed by averaging the forward and backward perturbations with respect to Δx changes in N noncloud properties. The centered differences for all N variables are computed for both clear-sky and all-sky conditions. Cloud contributions are then computed by

$$\delta F_{\Delta \text{cld}} = \Delta \text{CRE} - \sum_{i=1}^{N} \left(\delta F_{\Delta x_i, \text{all}} - \delta F_{\Delta x_i, \text{clr}} \right)$$
 (7)

where Δ CRE (total area clear-sky) is the anomaly in the cloud radiative effect derived from the Edition 4.2.1 EBAF data product. The second term on the right side of Eq. 7 is to subtract noncloud variables' (i.e., temperature, water vapor, trace gases, aerosol, and

solar constant) contributions to Δ CRE (70). We compute these perturbations using 1° × 1° gridded monthly hourly means and anomalies from gridded monthly hourly climatological means. The climatological means are computed from July 2005 through June 2015.

As explained earlier, surface, atmosphere, cloud, and aerosol properties are adjusted to match computed regional monthly mean TOA irradiances with CERES-derived TOA irradiances through bias corrections and adjustments from a Lagrange multiplier process described by Kato *et al.* (2). As in (27), these same corrections to skin temperature, surface air temperature, upper tropospheric relative humidity, precipitable water, aerosol optical depth, and surface albedo are applied to the PRP calculation inputs.

Supplementary Materials

This PDF file includes: Supplementary Text Figs. S1 to S3

Tables S1 and S2 References

REFERENCES AND NOTES

- G. L. Stephens, J. Li, M. Wild, C. A. Clayson, N. Loeb, S. Kato, T. L'Ecuyer, P. W. Stackhouse Jr., M. Lebsock, T. Andrews, An update on Earth's energy balance in light of the latest global observations. *Nat. Geosci.* 5, 691–696 (2012).
- S. Kato, F. G. Rose, D. A. Rutan, T. J. Thorsen, N. G. Loeb, D. R. Doelling, X. Huang, W. L. Smith, W. Su, S.-H. Ham, Surface irradiances of Edition 4.0 Clouds and the Earth's Radiant Energy System (CERES) Energy Balanced and Filled (EBAF) data product. *J. Clim.* 31, 4501–4527 (2018).
- A. Slingo, J. M. Slingo, The response of a general circulation model to cloud longwave radiative forcing. l: Introduction and initial experiments. Q. J. Roy. Meteorol. Soc. 114, 1027–1062 (1988)
- D. A. Randall, Harshvardhan, D. A. Dazlich, T. G. Corsetti, Interactions among radiation, convection, and large-scale dynamics in general circulation model. J. Atmos. Sci. 46, 1943–1970 (1989).
- S. C. Sherwood, V. Ramanathan, T. P. Barnett, M. K. Tyree, E. Roeckner, Response of an atmospheric general circulation model to radiative forcing of tropical clouds. *J. Geophys. Res.* 99, 20829–20845 (1994).
- T. Crueger, B. Stevens, The effect of atmospheric radiative heating by clouds on the Madden-Julian Oscillation. J. Adv. Model. Earth Syst. 7, 854–864 (2015).
- W. B. Rossow, Y.-C. Zhang, Calculation of surface and top of atmosphere radiative fluxes from physical quantities based on ISCCP data sets 2. Validation and first results. *J. Geophys. Res.* 100, 1167–1197 (1995).
- E. Raschke, A. Ohmura, W. B. Rossow, B. E. Carlson, Y.-C. Zhang, C. Stubenrauch, M. Kottek, M. Wild, Cloud effects on the radiation budget based on ISCCP data (1991 to 1995). Int. J. Climatol. 25, 1103–1125 (2005).
- N. G. Loeb, D. R. Doelling, H. Wang, W. Su, C. Nguyen, J. G. Corbett, L. Liang, C. Mitrescu, F. Rose, S. Kato, Clouds and the Earth Radiant Energy System (CERES) Energy Balanced and Filled (EBAF) Top-of-Atmosphere (TOA) Edition-4.0 data product. J. Clim. 31, 895–918 (2018).
- K. E. Trenberth, J. T. Fasullo, J. Kiehl, Earth's global energy budget. *Bull. Amer. Meteor. Soc.* 90, 311–324 (2009).
- M. Wild, D. Folini, C. Schar, N. Loeb, E. G. Dutton, G. Konig-Langlo, The global energy balance from a surface perspective. Clim. Dyn. 40, 3107–3134 (2013).
- T. L'Ecuyer, H. K. Beaudoing, M. Rodell, W. Olson, B. Lin, S. Kato, C. A. Clayson, E. Wood, J. Sheffield, R. Adler, G. Huffman, M. Bosilovich, G. Gu, F. Robertson, P. R. Houser, D. Chambers, J. S. Famiglietti, E. Fetzer, W. T. Liu, X. Gao, C. A. Schlosser, E. Clark, D. P. Letternmaier, K. Hilburn, The observed state of the energy budget in the early 21st century. J. Clim. 28, 8319–8346 (2015).
- R. P. Allan, C. Liu, M. Zahn, D. A. Lavers, E. Koukouvagias, A. Bodas-Salcedo, Physically constraint responses of the global atmospheric hydrological cycle in models and observations. Surv. Geophys. 35, 533–552 (2014).
- I. M. Held, B. J. Soden, Robust responses of the hydrological cycle to global warming. J. Climate 19, 5686–5699 (2006).
- 15. P. R. Allan, K. M. Willett, V. O. John, T. Trent, Global changes in water vapor. J. Geophys. Res. Atmos. 127, e2022JD036728 (2022).
- M. R. Allen, W. J. Ingram, Constrains on future changes in climate and the hydrologic cycle. Nature 419, 224–232 (2002).

- M. J. Webb, A. P. Lock, F. H. Lambert, Interactions between hydrological sensitivity, radiative cooling, stability, and low-level cloud amount feedback. J. Climate 31, 1833–1850 (2018)
- N. Siler, G. R. Roe, K. C. Armour, N. Feldl, Revisiting the surface-energy-flux perspective on the sensitivity of global precipitation on climate change. Clim. Dyn. 52, 3983–3995 (2019).
- J. F. B. Mitchell, C. A. Wilcon, W. M. Cunington, On Co² climate sensitivity and model dependence of results. Q. J. Roy. Meteorol. Soc. 113, 293–322 (1987).
- G. Myhre, B. H. Samset, Ø. Hodnebrog, T. Andrews, O. Boucher, G. Faluvegi, D. Fläschner, P. M. Forster, M. Kasoar, V. Kharin, A. Kirkevåg, J.-F. Lamarque, D. Olivié, T. B. Richardson, D. Shawki, D. Shindell, K. P. Shine, C. W. Stjern, T. Takemura, A. Voulgarakis, Sensible heat has significantly affected the global hydrological cycle over the historical period. *Nat. Commun.* 9, 1922 (2018).
- P. R. Allan, M. Barlow, M. P. Byrne, A. Cherchi, H. Douville, H. J. Fowler, T. Y. Gan, A. G. Pendergrass, D. Rosenfeld, A. L. S. Swann, L. J. Wilcox, O. Zolina, Advances in understanding large-scale responses of the water cycle to climate change. *Ann. N. Y. Acad. Sci.* **1472**, 49–75 (2020).
- R. F. Adler, G. Guojun, M. Sapoano, J.-J. Wang, G. J. Huffman, Global precipitation: Means, variations and trends during the satellite era (1979-2014). Surv. Geophys. 38, 679–699 (2017).
- G. Gu, R. F. Adler, Observed variability and trends in global precipitation during 1979-2020. Clim. Dyn. 61, 131–150 (2023).
- A. C. Naegele, D. A. Randall, Geographical and seasonal variability of cloud-radiative feedbacks on precipitation. J. Geophys. Res. Atmos. 124, 684–699 (2019).
- S. Kato, D. A. Rutan, F. G. Rose, T. E. Caldwell, S.-H. Ham, A. Radkevich, T. J. Thorsen,
 A. Viudez-Mora, D. Follmore, X. Huang, Uncertainty in satellite-derived surface irradiances and challenges in producing surface radiation budget climate data record. *Remote Sens.* 12, doi.org/10.3390/rs12121950 (2020).
- B. D. Santer, T. M. L. Wigley, J. S. Boyle, D. J. Gaffen, J. J. Hnilo, D. Nychka, D. E. Parker, K. E. Taylor, Statistical significance of trends and trend differences in layer-average atmospheric temperature time series. J. Geophys. Res. 105, 7337–7356 (2000).
- N. G. Loeb, G. C. Johnson, T. J. Thorsen, J. M. Lyman, F. G. Rose, S. Kato, Satellite and ocean data reveal marked increase in Earth's heating rate. *Geophys. Res. Lett.* 48, e2021GL093047 (2021).
- N. G. Loeb, F. G. Rose, S. Kato, D. A. Rutan, W. Su, H. Wang, D. R. Doelling, W. L. Smith, A. Gettelman, Towards a consistent definition between satellite and model clear-sky, radiative fluxes. J. Clim. 33, 61–75 (2020).
- N. G. Loeb, T. J. Thorsen, J. R. Norris, H. Wang, W. Su, Changes in Earth's energy budget during and after the "pause" in global warming: An observational perspective. *Climate* 6, 62 (2018).
- C. L. Parkinson, N. E. DiGirolamo, Sea ice extents continue to set new records: Arctic, Antarctic, and global results. Remote Sens. Environ. 267, 112753 (2021).
- R. Philipona, B. Dürr, C. Marty, A. Ohmura, M. Wild, Radiative forcing—Measured at Earth's surface – corroborate the increasing greenhouse effect. *Geophys. Res. Lett.* 31, doi. org/10.1029/2003GL018765 (2004).
- R. P. Allan, Examination of relationships between clear-sky longwave radiation and aspects of the atmospheric hydrological cycle in climate models, reanalyses, and observations. J. Clim. 22, 3127–3145 (2009).
- R. P. Allan, Combining satellite data and models to estimate cloud radiative effect at the surface and in the atmosphere. Meteorol. Appl. 18, 324–333 (2011).
- S. Kato, F. G. Rose, D. A. Rutan, T. P. Charlock, Cloud effects on meridional atmospheric energy budget estimated from Clouds and the Earth's Radiant Energy System (CERES) data. J. Clim. 21, 4223–4241 (2008).
- S. Kato, Interannual variability of the global radiation budget. J. Clim. 22, 4893–4907 (2009).
- Z. Jin, T. P. Charlock, W. L. Smith Jr., K. Rutledge, Al parameterization of ocean surface albedo. Geophys. Res. Lett. 31. doi.org/10.1029/2004GL021180 (2004).
- M. Sidran, Broadband reflectance and emissivity of specular and rough water surfaces. Appl. Optics 20, 3176–3183 (1981).
- S.-H. Ham, S. Kato, F. G. Rose, Correction of ocean hemispherical spectral reflectivity for longwave irradiance computations. J. Quant. Spectrosc. Radiat. Transf. 171, 57–65 (2016).
- S. Kato, N. G. Loeb, F. G. Rose, S.-H. Ham, T. J. Thorsen, D. A. Rutan, W. F. Miller,
 T. E. Caldwell, D. R. Doelling, S. Sun-Mack, Seamless continuity in CERES Energy balanced
 and Filled (EBAF) surface radiation budget across multiple satellites. *J. Climate* 38,
 2461–2478 (2025).
- C. Bourgoin, R. Beuchle, A. Branco, J. Carreieas, G. Ceccherini, D. Oom, J. San-Miguel-Ayanz, F. Sedano, Extensive fire-driven degradation in 2024 marks worst Amazon forest disturbance in over two decades. *EGUsphere*, doi.org/10.5194/ egusphere-2025-1823 (2015).
- 11. M. Previdi, Radiative feedbacks on global precipitation. *Environ. Res. Lett.* **5**, 05221 (2010).
- N. G. Loeb, S.-H. Ham, R. P. Allan, T. J. Thorsen, B. Meyssignac, S. Kato, G. C. Johnson, J. M. Lyman, Observational assessment of changes in Earth's energy imbalance since 2000. Surv. Geophys. 45, 1757–1783 (2024).

SCIENCE ADVANCES | RESEARCH ARTICLE

- L. Millán, M. L. Santee, A. Lambert, N. J. Livesey, F. Werner, M. J. Schwartz, H. C. Pumphrey, G. L. Manney, Y. Wang, H. Su, L. Wu, W. G. Read, L. Froidevaux, The Hunga Tonga-Hunga Ha'apai hydration of the stratosphere. *Geophys. Res. Lett.* 49, e2022GL099381 (2022).
- H. Vömel, S. Evan, M. Tully, Water vapor injection into the stratosphere by Hunga Tonga-Hunmga Ha'apai. Science 377, 1444–1447 (2022).
- 45. S. Jenkins, C. Smith, M. Allen, R. Grainger, Tonga eruption increases change of temporary surface temperature anomaly above 1.5 °C. *Nat. Clim. Chang.* **13**, 127–129 (2023).
- S. Kato, K.-M. Xu, T. Wong, N. G. Loeb, F. G. Rose, K. E. Trenberth, T. J. Thorsen, Investigation
 of the bias in column integrated atmospheric energy balance using cloud objects. *J. Clim.*29, 7435–7452 (2016).
- M. Mayer, L. Haimberger, J. M. Edward, P. Hyder, Toward consistent diagnostics of the coupled atmosphere and ocean energy budgets. J. Clim. 30, 9225–9246 (2017).
- 48. W. Berg, T. L'Ecuyer, C. Kummerow, Rainfall climate regimes: Relationship of regional TRMM rainfall biases to the environment. *J. Appl. Meteol. Climatol.* **45**, 434–454 (2006).
- J. M. Haywood, N. Bellouin, A. Jones, O. Boucher, M. Wild, K. P. Shine, The roles of aerosol, water vapor and cloud in future global dimming/brightening. *J. Geophys. Res.* 116, doi. org/10.1029/2011JD016000 (2011).
- K. von Schuckmann, A. Minière, F. Gues, F. J. Cuesta-Valero, G. Kirchengast,
 G. S. Adusumilli, F. Straneo, M. Ablain, R. P. Allan, P. M. Barker, H. Beltrami, A. Blazquez,
 T. Boyer, L. Cheng, J. Church, D. Desbruyeres, H. Dolman, C. M. Domingues,
 A. García-García, D. Giglio, J. E. Gilson, M. Gorfer, L. Haimberger, M. Z. Hakuba,
 S. Hendricks, S. Hosoda, G. C. Johnson, R. Killick, B. King, N. Kolodziejczyk, A. Korosov,
 G. Krinner, M. Kuusela, F. W. Landerer, M. Langer, T. Lavergne, I. Lawrence, Y. Li, J. Lyman,
 F. Marti, B. Marzeion, M. Mayer, A. H. MacDougall, T. McDougall, D. P. Monselesan,
 J. Nitzbon, I. Otosaka, J. Peng, S. Purkey, D. Roemmich, K. Sato, K. Sato, A. Savita,
 A. Schweiger, A. Shepherd, S. I. Seneviratne, L. Simons, D. A. Slater, T. Slater, A. K. Steiner,
 T. Suga, T. Szekely, W. Thiery, L.-M. Timmermans, I. Vanderkelen, S. E. Wjiffels, T. Wu,
 M. Zemp, Heat stored in the Earth system 1960–2020: Where does the energy go?
 Earth Syst. Sci. Data 15, 1675–1709 (2023).
- M. Mayer, S. Kato, M. Bosilovich, P. Bechtold, J. Mayer, M. Schröder, A. Behrangi, M. Wild,
 S. Kobayashi, Z. Li, B. Roberts, T. L'Ecuyer, Assessment of atmospheric and surface energy budget using observation-based data products. Surv. Geophys. 45, 1827–1854 (2024).
- B. A. Wielicki, B. R. Barkstrom, E. F. Harrison, R. B. Lee III, G. L. Smith, J. E. Cooper, Clouds and the Earth's Radiant Energy System (CERES): An Earth Observing System Experiment. Bull. Amer. Meteorol. Soc. 77. 853–868 (1996).
- 53. B. Cairns, Diurnal variations of cloud from ISCCP data. Atmos. Res. 37, 133-146 (1995).
- W. B. Rossow, R. A. Schiffer, ISCCP cloud data products. Bull. Am. Meteorol. Soc. 72, 2–20 (1991).
- Y. C. Zhang, W. B. Rossow, A. A. Lacis, Calculation of surface and top of atmosphere radiative fluxes from physical quantities based on ISCCP data set I, Method and sensitivity to input data uncertainties. J. Geophys. Res. 100, 1149–1165 (1995).
- N. G. Loeb, D. R. Doelling, S. Kato, W. Su, P. E. Mlynczak, J. C. Wilkins, Continuity in top-of-atmosphere earth radiation budget observations. *J. Climate* 37, 6093–6108 (2024).
- W. Su, J. Corbett, Z. Eitzen, L. Liang, Next-generation angular distribution models for top-of-atmosphere radiative flux calculation from CERES instruments: Methodology. *Atmos. Meas. Tech.* 8, 611–632 (2015).
- P. Minnis, S. Sun-Mack, Y. Chen, F.-L. Chang, C. R. Yost, W. L. Smith Jr., P. W. Heck, R. F. Arduini, S. T. Bedka, Y. Yi, G. Hong, Z. Jin, D. Painemal, R. Palikonda, B. R. Scarino, D. A. Spangenberg, R. A. Smith, Q. Z. Trepte, P. Yang, Y. Xie, CERES MODIS cloud product retrievals for Edition 4-Part I: Algorithm changes. *IEEE Trans. Geosci. Remote Sens.* 59, 2744–2780 (2020).
- R. C. Levy, S. Mattoo, L. A. Munchak, L. A. Remer, A. M. Sayer, F. Patadia, N. C. Hsu, The collection 6 MODIS aerosol products over land and ocean. *Atmos. Meas. Tech.* 6, 2989–3034 (2013).
- N. C. Hsu, M.-J. Jeong, C. Bettenhausen, A. M. Sayer, R. Hansell, C. S. Seftor, J. Huang, S.-C. Tsay, Enhanced deep blue aerosol retrieal algorithm: The second generation. *J. Geophys. Res.* 118, 9296–9315 (2013).
- R. C. Levy, L. A. Munchak, S. Mattoo, F. Patadia, L. A. Remer, R. E. Holz, Towards a long-term global aerosol optical depth records: Applying a consistent aerosol retrieval algorithm to MODIS and VIIRS-observed reflectance. *Atmos. Meas. Tech.* 8, 4083–4110 (2015).

- J. Lee, N. C. Hsu, W. V. Kim, A. M. Sayer, S.-C. Tsay, VIIRS version 2 Deep Blue aerosol products. J. Geophys. Res. Atmos. 129, e2023JD040082 (2024).
- D. R. Doelling, N. G. Loeb, D. F. Keyes, M. L. Mordeen, D. Morstad, C. Nguyen, B. A. Wielicki, D. F. Young, Geostationary enhanced temporal interpolation for CERES flux products. J. Atmospheric Ocean. Technol. 30, 1072–1090 (2013).
- T. J. Thorsen, S. Kato, N. G. Loeb, F. G. Rose, Observation-based decomposition of radiative perturbations and radiative kernels. *J. Climate* 31, 10039–10058 (2018).
- G. J. Huffman, R. F. Adler, A. Behrangi, D. T. Bolvin, E. J. Nelkin, G. Guojun, M. R. Ehsani, The new version 3.2. Global Precipitation Climatology Project (GPCP) monthly and daily precipitation products. J. Climate 36, 7635–7655 (2023).
- G. J. Huffman, A. Behrangi, D. T. Bolvin, E. J. Nelkin, GPCP Version 3.2 Satellite-Gauge (SG) Combined Precipitation Data Set, Edited by G. J. Huffman, A. Behrangi, D. T. Bolvin, E. J. Nelkin, Greenbelt, Maryland, USA, Goddard Earth Sciences Data and Information Services Center (GES DISC) (2022), 10.5067/MEASURES/GPCP/DATA304.
- G. Gu, R. Adler, Variability and trends in tropical precipitation intensity in observations and climate models. Clim. Dyn. 62, 7429–7443 (2024).
- S. Kato, N. G. Loeb, J. T. Fasullo, K. E. Trenberth, P. H. Lauritzen, F. G. Rose, D. A. Rutan, M. Satoh, Regional energy and water budget of the atmosphere over ocean. *J. Clim.* 34, 4189–4205 (2021).
- R. T. Wetherald, S. Manabe, Cloud feedback processes in a general circulation model. J. Atmos. Sci. 45, 1397–1416 (1988).
- B. J. Soden, I. M. Held, R. Colman, K. M. Shell, J. T. Kiehl, C. A. Shields, Quantifying climate feedbacks using radiative kernels. J. Clim. 21, 3504–3520 (2008).
- K. Wolter, M. S. Timlin, El Niño/Southern Oscillation behaviour since 1871 as diagnosed in an extended multivariate ENSO index (MEl.ext). Intl. J. Climatol. 31, 1074–1087 (2011).
- R. W. Reynolds, T. M. Smith, C. Liu, D. B. Chelton, K. S. Casey, M. G. Schlax, Daily high-resolution-blended analysis for sea surface temperature. *J. Clim.* 20, 5473–5496 (2007).
- C. Donlon, I. Robinson, K. S. Casey, J. Vazquez-Cuervo, E. Armstrong, O. Arino,
 C. Gentemann, D. May, P. LeBorgne, J. Pillé, I. Barton, H. Geggs, D. J. S. Poulter,
 C. J. Marchant, A. Bingham, S. Heinz, A. Harris, G. Wick, B. Emery, P. Minnett, R. Evans,
 D. Llewellyn-Jones, C. Mutlow, R. W. Reynolds, H. Kawamura, N. Rayner, The global ocean
 data assimilation experiment high-resolution sea surface temperature pilot project.
 Bull. Amer. Meteor. Soc. 88, 1197–1214 (2007).
- M. G. Bosilovich, S. Akella, L. Coy, R. Cullather, C. Draper, R. Gelaro, R. Kovach, Q. Liu, A. Molod, P. Norris, K. Wargan, W. Chao, R. Reichle, L. Takacs, Y. Vikhliaev, S. Bloom, A. Collow, S. Firth, G. Labow, G. Partyka, S. Pawson, O. Reale, S. D. Schubert, M. Suarez, MERRA-2: Initial evaluation of the climate. NASA 43, 1–139 (2015).

Acknowledgments: We thank M. Bosilovich of NASA Goddard Space Flight Center for pointing out surface temperature and skin temperature issues in MERRA-2 and the reviewers for providing constructive comments. Funding: This work has been supported by the NASA CERES project. R.P.A. received support from the Research Councils UK (RCUK) National Centre for Earth Observation (grant numbers NE/RO16518/1 and NE/Y006216/1). M.M.'s efforts were supported by ESA contracts ref. 4000145298/24/I-LR (MOTECUSOMA) and ref. 4000147586/I/25-LR (ESA-CCI Surface Ocean Heat Flux). Author contributions: Conceptualization: S.K., T.J.T., N.G.L., R.P.A., and M.M. Methodology: S.K., T.J.T., F.G.R., N.G.L., S.-H.H., D.A.R., Z.L., M.M., R.F.A., G.G., S.L., and J.L. Investigation: S.K. and T.J.T. Writing—original draft: S.K. Writing—review and editing: S.K., T.J.T., N.G.L., S.-H.H., D.A.R., Z.L., M.M., R.P.A., R.F.A., G.G., S.L., and J.L. Competing interests: The authors declare that they have no competing interests. Data and materials availability: CERES data are available from https://ceres.larc. nasa.gov/data/, GPCP data are available from https://daac.gsfc.nasa.gov/datasets/ GPCPMON_3.2/summary?keywords=GPCPMON_3.2, and ERA5 data are available from https:// cds.climate.copernicus.eu/cdsapp#!/dataset/derived-reanalysis-energy-moisturebudget?tab=overview and https://cds.climate.copernicus.eu/cdsapp#!/dataset/reanalysisera5-single-levels-monthly-means?tab=overview.

Submitted 19 May 2025 Accepted 16 September 2025 Published 15 October 2025 10.1126/sciadv.adz1292